An Anthracene-based Precursor for Sulfur Monoxide Delivery: Thermal Release, Spectroscopic Identification and Transfer Reactivity

Maximilian Joost, Matthew Nava, Wesley J. Transue, M. A. Martin-Drumel, Michael Mccarthy, David Patterson, Christopher C Cummins

An Anthracene-based Precursor for Sulfur Monoxide Delivery: Thermal Release, Spectroscopic Identification and Transfer Reactivity

Maximilian Joost[a], Matthew Nava[a], Wesley J. Transue[a], Marie-Aline Martin-Drumel[b], Michael C. McCarthy[c], David Patterson[d,e], and Christopher C. Cummins[a,1]

[a]Department of Chemistry, Massachusetts Institute of Technology, 77 Massachusetts Avenue, Cambridge, MA 02139, USA.; [b]Institut des Sciences Moléculaires d'Orsay, CNRS, Bât. 210, Université Paris–Sud, 91405 Orsay, France.; [c]Harvard-Smithsonian Center for Astrophysics, 60 Garden Street, Cambridge, MA 02138, USA.; [d]Department of Physics, Harvard University, 17 Oxford Street, Cambridge, MA 02138, USA.; [e]Current address: Department of Physics, University of California, Santa Barbara, Santa Barbara, CA 93106, USA.

This manuscript was compiled on February 27, 2018

Sulfur monoxide (SO) is a highly reactive molecule and thus eludes bulk isolation. We report here on synthesis and reactivity of a molecular precursor for SO generation, namely 7-sulfinylamino-7-azadibenzonorbornadiene (1). This compound has been shown to fragment readily, driven by dinitrogen expulsion and anthracene formation upon heating in the solid state and in solution, releasing sulfur monoxide at mild temperatures (< 100 °C). The generated SO was detected in the gas phase by mass spectrometry and rotational spectroscopy. In solution, 1 allows for SO transfer to organic molecules as well as transition metal complexes.

sulfur monoxide | molecular precursor | reactive species | species of astrochemical interest | microwave spectroscopy

In contrast to the ubiquitous and well-studied chemistry of earth-abundant dioxygen,(1) the chemistry of its heavier, valence-isoelectronic analogue sulfur monoxide (SO) is hardly explored and has been relegated to a niche existence, which is certainly due to its high reactivity: SO is unstable under ambient conditions toward disproportionation to SO_2 and elemental S,(2) and eludes bulk isolation. However, in space SO can accumulate, and has been found in the interstellar medium,(3, 4) as well as in our solar system,(5–7) which is important to note considering that both O and S are biogenic elements.(8)

Fragmentation of suitable molecular precursors presents a potential entrypoint to explore the synthetic chemistry for such reactive species and opens new avenues for spectroscopic characterization.(9–16) In the case of SO, a limited number of synthetic precursors have been reported which allow thermal transfer of SO (Fig. 1): Well-investigated are the chemistry of episulfoxides (**A**),(17–20) a thiadiazepin *S*-oxide (**B**),(21) trisulfide oxides (**C**),(22, 23) thianorbornadiene-*S*-oxides (**D**),(24) and *N*-sulfinylamine phosphinoborane adducts (**E**).(25) In explaining the SO-transfer reactions of some of these substances, the intermediacy of free SO is assumed, while for others the precursors fragment likely via associative mechanisms.

Our group has a longstanding interest in small, reactive species such as P_2,(9–11) AsP,(12) HCP,(13) phosphinidenes(14, 15) and dimethylgermylene,(16) generated by mild thermal activation of suitable precursors. The driving force of anthracene ($C_{14}H_{10}$, **A**) expulsion for the release of highly reactive molecules and subsequent characterization and synthetic transfer has been amply capitalized on.(13, 14, 26–31) Against this backdrop and our reasoning that an additional N_2 unit should further increase the energy of the ground state of the precursor molecule, we envisioned our synthetic target, 7-sulfinylamino-7-azadibenzonorbornadiene, OSN_2**A** (**1**), as promising for SO release, simultaneously with **A** and dinitro-

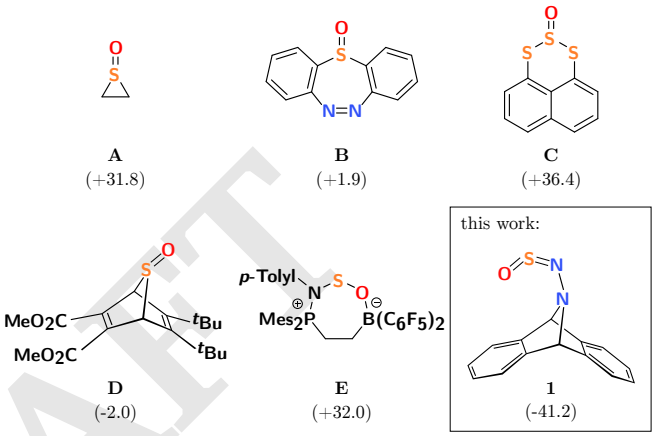

Fig. 1. Selection of previously reported compounds capable of SO transfer (**A**-**E**) and the anthracene-based sulfinylhydrazine **1** described herein. In parentheses: computed Gibbs free energies (in kcal·mol^{-1} at 298.15 K, at the B3LYP-D3BJ/Def2-TZVP level of theory) for singlet SO loss and formation of the respective coproducts.

Significance Statement

The generation of highly reactive molecules under controlled conditions is desirable as it allows to explore synthetic chemistry and enables spectroscopic studies of such elusive species. We report here on the synthesis and reactivity of a precursor molecule that readily fragments with concomitant expulsion of dinitrogen and anthracene to release the highly reactive sulfur monoxide (SO), a compound of interest for both synthetic chemists and astrochemists.

M.J., M.N., W.J.T. and C.C.C. designed research; M.J., M.N., W.J.T., M.M.D. and D.P. performed research and analyzed data, M.J., M.N. and C.C.C. wrote the paper.

The authors declare no conflict of interest.

[1]To whom correspondence should be addressed. E-mail: ccummins mit.edu

gen formation. To probe this hypothesis, we compared the computed Gibbs free energies (B3LYP-D3BJ/Def2-TZVP) for singlet SO release from **A**–**E** and **1** (Fig. 1). Indeed, the formation of singlet SO was predicted to be thermodynamically strongly favorable only in case of **1**.

Free SO, amenable to spectroscopy, has been generated by electric discharge experiments of SO-containing gases (OCS, SO_2),(32) or using ethylene episulfoxide at high temperature (180 °C to 580 °C).(33) To the best of our knowledge, spectroscopic observation of free SO provided by mild thermolysis of a well-defined, solid, and easy-to-handle precursor compound has not been achieved. With **1**, we present now the synthesis of such a compound that fragments at ca. 95 °C in the solid state and allows for direct detection of sulfur monoxide in the gas phase. In addition, examples of SO transfer with this reagent in solution to both organic molecules and transition metal complexes are outlined.

Results and Discussion

The synthesis of **1** was achieved by reaction of Carpino's hydrazine (7-amino-7-azadibenzonorbornadiene, H_2N_2**A**),(30) with thionyl chloride in the presence of triethyl amine (Scheme 1).(34)

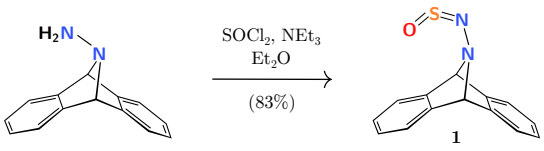

Scheme 1. Synthesis of **1**.

Compound **1** was isolated as a pale-yellow solid in very good yield (83%). In solution (benzene-d_6), the ^{1}H NMR chemical shift of the bridgehead protons at δ = 6.22 ppm, located 1.48 ppm downfield from that of H_2N_2**A**, is reflective of the strongly withdrawing effect of the sulfinyl group. Colorless crystals grew from a concentrated toluene solution of **1** layered with diethyl ether at –35 °C, and were subjected to X-ray diffraction analysis. The metrical data of the NNSO chain of **1** in the solid state (Fig. 2) compare well with the reported structures of sulfinyl hydrazines.(35–37) One bridgehead proton of the azanorbornadiene scaffold weakly interacts with the terminal oxygen atom, leading to a synperiplanar NNSO arrangement as observed for ^{i}Pr$_2$N$_2$SO.(36)

A thermogravimetric analysis (TGA) was performed to probe the potential release of SO. At 95 °C, a mass loss event of 30 wt% was observed, supporting the notion that N_2 and SO (11 wt% and 19 wt%, respectively) were released (see SI).

Eager to confirm the evolution of SO from **1** in accordance with the TGA experiment, direct spectroscopic observation of SO was sought. Detection of SO is difficult in condensed media and the gas phase due to its rapid self reaction culminating in the formation of SO_2 and polysulfides (Eq. 1).(2, 38, 39)

$$\begin{aligned} 2SO &\rightleftharpoons S_2O_2 \\ S_2O_2 + SO &\longrightarrow SO_2 + S_2O \\ 2S_2O &\longrightarrow SO_2 + S_3 \end{aligned} \qquad [1]$$

Due to the propensity for self reaction, SO is typically only generated and observed in high vacuum to minimize bimolecular reactivity and accordingly previous studies of molecular precursors for SO in condensed media relied on chemical trapping experiments and kinetic analysis to infer its intermediacy.

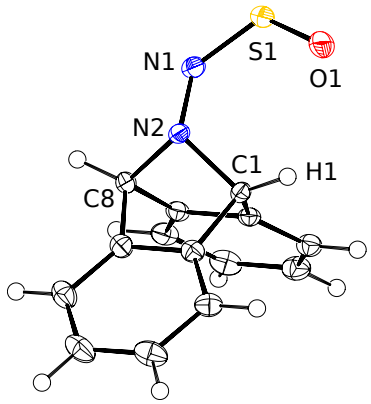

Fig. 2. Molecular structure of **1** in the solid state with thermal ellipsoids at the 50% probability level. Selected distances [Å] and angles [°]: N1-N2 1.353(3), N1-S1 1.544(2), S1-O1 1.466(2), O1-H1 2.432 (intramolecular), H1-O1 2.489 (intermolecular), N2-N1-S1 125.9(2), N1-S1-O1 118.2(1), S1-O1-H1 100.0, C1-N2-C8 96.0(2).

Thermolysis in a gas infrared (IR) cell under static vacuum (ca. 50 mTorr) led to the identification of SO_2 as the major gaseous product, in accord with loss of SO and subsequent disproportionation chemistry, but did not provide conclusive evidence for the intermediacy of SO (see SI).

For the detection of such short-lived species upon thermal decomposition of molecular precursors, molecular beam mass spectrometry (MBMS) has proven to be a valuable tool to analyze unstable gaseous products evolved from molecular precursors.(10, 13, 15) In case of thermolysis of **1** in the MBMS sample chamber, **A**, N_2 and SO were observed (Fig. 3). The differing results of the MBMS and gas IR experiments can be rationalized based upon differences in pressure when **1** is thermolyzed and the large disparity in the rate of data acquisition between the two methods (IR spectrum acquisition required several seconds).

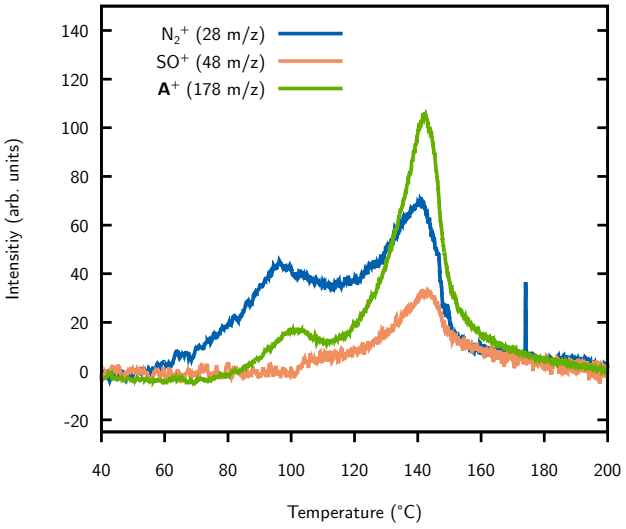

Fig. 3. Molecular beam mass spectrometry (MBMS) of **1**.

The direct observation of SO via mass spectrometry encouraged us to attempt as well its characterization by microwave spectroscopy. The rotational transitions of sulfur monoxide have been previously studied in detail, for ground electronic as well as the first excited state.(40, 41) Compound **1** was thermolyzed in a specially constructed solid sample holder directed at the entrance of a buffer-gas cell.(42) Gases evolved from **1** during heating enter the buffer-gas cell where they collide with gaseous helium at ca. 10 K. The collisions of the evolved gases with the helium rapidly cool the molecules which results in the rotational and vibrational cooling of the sample, simplifying their rotational spectra but also inhibiting bimolecular reactivity. After introduction and cooling of the fragment molecules, a microwave spectrum of the mixture was recorded (Fig. 4).

Next to characteristic transitions corresponding to S_2O ($2_{1,2} \leftarrow 3_{0,3}$, 13258.94 MHz)(43) and SO_2 ($1_{1,1} \leftarrow 2_{0,2}$, 12256.58 MHz),(44) $^3\Sigma^-$ SO ($1_2 \leftarrow 1_1$, 13043.7 MHz)(40) was detected. As for O_2, the triplet ($^3\Sigma^-$) is the most stable configuration for SO, with the closed-shell ($^1\Delta$) and open shell ($^1\Sigma^+$) singlets lying 18.2 kcal·mol^{-1} and 30.1 kcal·mol^{-1} above the ground state, respectively.(45) The transition for $^3\Sigma^-$ SO was split due to Earth's magnetic field and disappeared out of the spectral window in the presence of a strong external magnetic field. We are unable to verify the presence of the closed-shell singlet SO, because the lowest frequency transition at 42591.2315 MHz is out of range of the microwave instrument employed (12000 MHz–17500 MHz).(46) The observation of open-shell and closed-shell singlet electronic states of SO should be feasible in principle: The radiative lifetimes of these species were determined to be ca. 7 ms (exp. value; calc. 13.6 ms) and 450 ms (calc.), respectively.(47, 48) Singlet SO is thus sufficiently long-lived for detection with our apparatus with an approximate flight time of 2-3 ms assuming a reasonable molecular velocity in the gas phase (see SI).

In addition, we were able to identify the rotational transitions of **1** itself, which partially transferred without fragmentation into the gas phase. The pure rotational spectrum of **1** was analyzed using a variant of the Automated Microwave DOuble Resonance (AMDOR) technique.(49) The small differences between the experimentally obtained rotational constants and those recovered from calculations based on the geometry of **1** in the crystal structure, imply that the structure of **1** is nearly identical in the solid state and in the gas phase (see SI). The differences in the observed products of thermolysis of **1** highlights the complementary nature of the techniques utilized, but also illustrates how critical the thermolysis conditions are to what gases are evolved from **1**.

In order to comment on the thermolysis mechanism of **1**, a computational investigation at the RI-B2PLYP-D3(BJ)/Def2-TZVP level of theory was performed. A single-step fragmentation with concerted loss of singlet SO and N_2 from the anthracene platform was found, featuring a single transition state corresponding to the breaking of the C–N bond opposed to the sulfinylamino moiety. The minimum energy path across this transition state revealed no further stationary points en route to the final products: the structure collapsed in a concerted, asynchronous way with breaking of the N–S and of the second C–N bond. This is likely due to the NNSO intermediate not being a minimum on the potential energy surface.(50) This quasi-simultaneous breaking and making of bonds in this fragmentation process may be classified as a coarctate reaction, as defined by Herges.(51) While for pericyclic reactions the concerted breaking and forming of bonds occurs in a cyclic manner, coarctate processes describe bond rearrangements with a transition state topology of a constricted cycle. The constriction point is located at the coarctate atom(s) at which two bonds are broken and reformed in the transition state. In case of the fragmentation of **1** both N atoms are coarctate atoms. In this process, SO may indeed be released in its singlet state: the formation of **A**, N_2 and singlet SO is favored by –40.4 kcal·mol^{-1} with respect to the starting material.

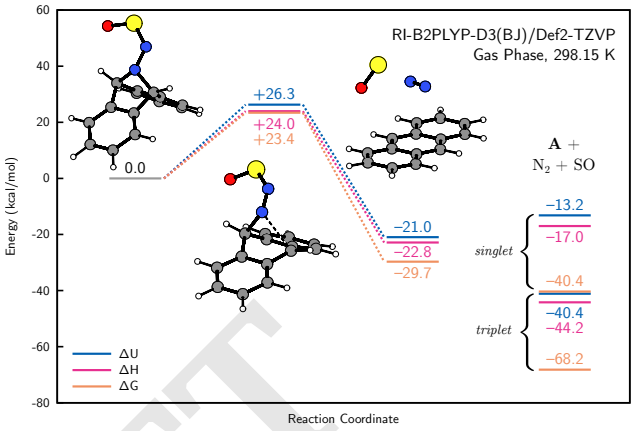

Fig. 5. Computed mechanism for the fragmentation of **1** (at the RI-B2PLYP-D3(BJ)/Def2-TZVP level of theory).

With evidence of SO release upon thermolysis in the solid state, we explored the reactivity of **1** in solution. Heating **1** in benzene-d_6 in a sealed tube led to its decomposition, indicated visually by a color change from colorless to yellow, likely due to production of sulfur. The sole product observable by ^{1}H NMR spectroscopy was **A**. This reaction obeyed a first-order rate law with $k_{obs} = (2.743 \pm 0.436) \times 10^{-4}$ s^{-1} at 80 °C in THF as determined by UV-Vis spectroscopy. This barrier corresponded to an activation barrier of $\Delta G^{\ddagger}(80\,^{\circ}\mathrm{C}) = 26.55(11)$ kcal·mol^{-1} according to the Eyring equation, similar to the calculated value of $\Delta G^{\ddagger}_{calc}(80\,^{\circ}\mathrm{C}) = 23.3$ kcal·mol^{-1}.

To assess the possibility of SO transfer from **1** to an acceptor, various representative reaction partners were employed. We focused first on organic compounds suitable for SO trapping such as quinones and olefins (Scheme 2). Compound **1** was heated with with 3,5-di-*tert*-butyl-1,2-quinone for 24 h to 70 °C to convert quantitatively to the corresponding known sulfite.(52)

Several SO-releasing precursors are capable of SO addition to 1,3-dienes.(18, 21–24, 53, 54) Heating of **1** with an excess (5 equiv) of 2,3-dimethyl-1,3-butadiene (DMB) led to decomposition of **1** without thiophene-*S*-oxide formation. However, when performing the reaction at 80 °C in neat DMB, this SO-transfer product was observed (60%). Similarly, transfer of SO to 1,3-cyclohexadiene was successful. Likely due to the locked *cisoid* conformation of the double bond, just a 5-fold excess of this diene was sufficient to lead to formation of 7-oxo-7-thianorbornene (59%).(23) Thermal SO transfer to other olefins or alkynes was unsuccessful: reactions employing *cis*-stilbene, styrene or phenyl acetylene in excess did not provide the respective addition products.

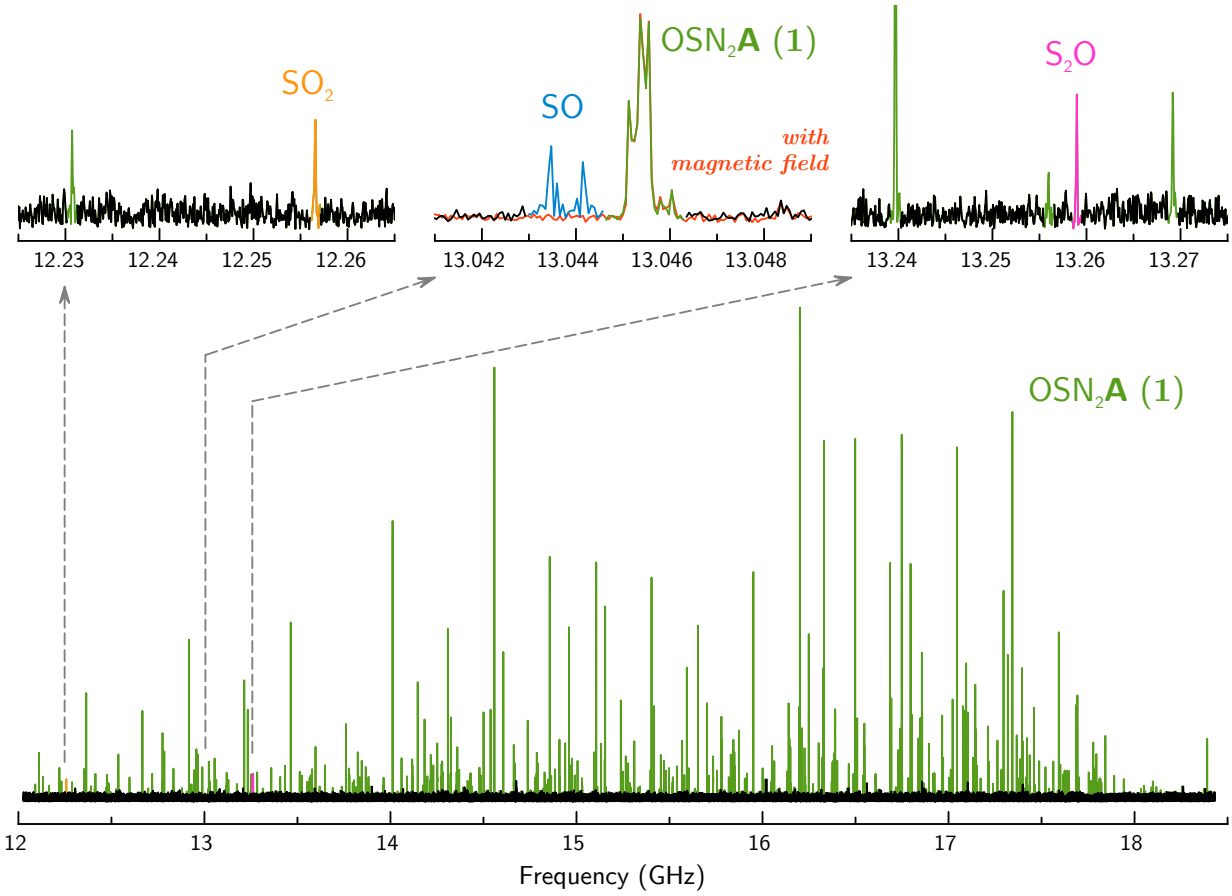

Fig. 4. Microwave spectrum of the compounds released during the thermal heating of **1**. Transitions belonging to **1**, SO_2, SO, and S_2O are indicated in green, orange, blue, and pink, respectively, while the remaining unassigned portions of the spectrum appear in black. The spectrum showing the SO transition was the result of a deeper integration and an additional spectrum was recorded in the same conditions but under the influence of an external magnetic field (in red) to confirm the open-shell nature of the carrier of the lines assigned to SO. In presence of the magnetic field, lines of SO are not visible (as expected for a species with unpaired electrons in a $^3\Sigma$ ground electronic state) while the transitions of **1** (closed shell) are unaffected.

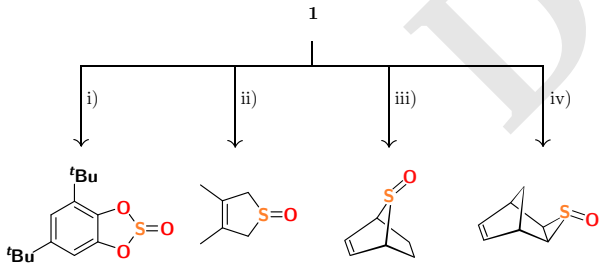

Scheme 2. Transfer of sulfur monoxide from **1**. i) 3,5-di-*tert*-butyl-1,2-quinone (1 equiv), benzene, 70 °C , 24 h (quant.); ii) DMB (neat), 80 °C , 16 h (60%); iii) 1,3-cyclohexadiene (5 equiv), benzene, 70 °C , 24 h (59%); iv) norbornadiene (10 equiv), benzene, 25 °C , 16 h (55%).

Contrasting reactivity of **1** towards norbornadiene yielded the corresponding thiirane (55%): Addition of SO occurred at 25 °C (16 h), well below the temperature required for fragmentation of **1**, and thus does not involve free SO, but rather proceeds via an associative mechanism. The SO transfer from **1** to transition metal complexes occurs similarly (Scheme 3). Stirring a solution of **1** and $[RuCl(Cp^*)(PCy_3)]$ ($Cp^* = \eta^5$-C_5Me_5) in THF at 25 °C for 30 min led to a gradual color change from blue to red-brown. After removal of **A**, the known SO ruthenium complex $[RuCl(Cp^*)(SO)(PCy_3)]$ was isolated (82%).(55, 56) Compound **1** also reacted with the anionic ruthenium complex $[Na(DME)_3]_2[Ru(N_4Me_8)]$ ($H_4N_4Me_8$ = octamethylporphyrinogen)(57) to give $[Na(DME)_3][Ru(N_4Me_8)(SO)]$ (**2**), obtained in 51% yield after removal of anthracene and selective crystallization as a brown-orange solid.

Cooling a solution of this compound in THF and DME to –35 °C yielded dark-orange crystalline blocks. An X-ray diffraction analysis revealed a dimeric structure, with sodium ions bridging two units of the $[Ru(N_4Me_8)(SO)]^{2-}$ platform (Fig. 6). These units feature the ruthenium center in a square-pyramidal environment in which the SO ligand occupies the apical position. The Ru—S bond [2.0282(8) Å] is slightly shorter and the S–O bond [1.503(2) Å] slightly longer than in a related Ru(II)-sulfur monoxide complex [2.0563(11) Å and 1.447(3) Å), respectively].(58) Terminal sulfur monoxide transition metal complexes generally show a strong SO stretch around 1046–1126 cm^{-1}.(54, 55, 58, 59) Analysis of the IR spectrum of **2** revealed a band at 1021 cm^{-1} assigned to the

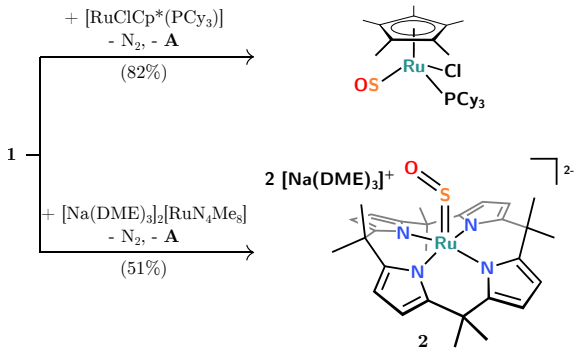

Scheme 3. Transfer of SO from **1** to ruthenium complexes.

SO stretching vibration. Both this notable red-shift with regard to values for related compounds as well as the metrical data for **2** are in accord with strong backbonding from Ru to the SO ligand due to the electron-rich porphyrinogen ligand. Coordination of the sodium cations to the oxygen atom of ligated SO may enhance this effect.

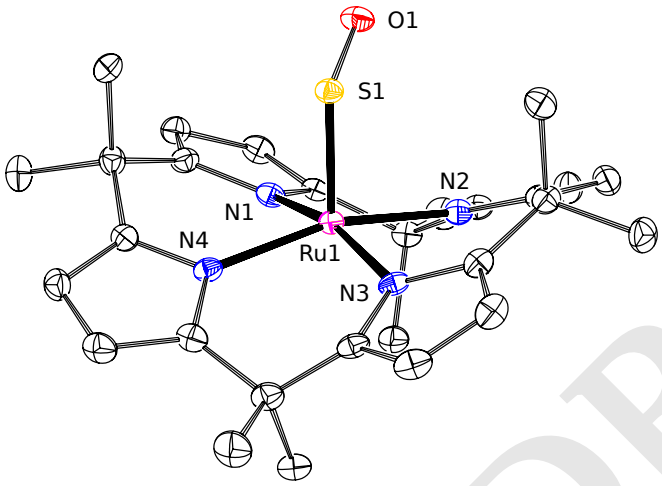

Fig. 6. Molecular structure of **2** in the solid state with thermal ellipsoids at the 50% probability level. SO-coordinated sodium cation and separate sodium tris(1,2-dimethoxyethane) cation, as well as one cocrystallized THF solvent molecule have been omitted for clarity. Selected distances [Å] and angles [°]: Ru1-S1 2.0282(8), S1-O1 1.503(2), Ru1-N 2.044 (avg); Ru1-S1-O1 118.17(11).

We did not observe selective reaction of **1** with *N*-heterocyclic carbenes to give the corresponding sulfines. However, heating a mixture of **1** and a phosphine (PPh_3 or P^tBu_3) in benzene gave about equimolar mixtures of the respective phosphine oxides and phosphine sulfides via formal splitting of SO.(25)

Conclusion. We have demonstrated here a well-controlled synthetic route to SO by thermal decomposition of **1**. Taking reactivity, computational studies and spectroscopic detection of $^3\Sigma^-$ SO into consideration, it is believed that **1** generates $^1\Delta$ SO upon thermolysis. $^3\Sigma^-$ SO is detected by microwave spectroscopy, possibly originating from a small amount of $^1\Delta$ SO that has had enough time to phosphoresce into the lower energy triplet ground state. Regardless of the spin state of the SO evolved from **1**, this study firmly establishes that SO is in fact released from the molecular precursor, illustrating the power of synthesis in combination with spectroscopy to shed light on reactive intermediates of general importance.

Methods. Experimental and computational details, and crystallographic information are included in *SI Methods*.

ACKNOWLEDGMENTS. The authors thank Prof. Robert Field (MIT) for inspiring discussions. This material is based on research supported by the National Science Foundation under CHE-1362118. D.P. acknowledges support by the NSF Instrument Development for Biological Research program (NSF award 134076-5101408). M.J. thanks the Alexander von Humboldt foundation for a Feodor Lynen postdoctoral fellowship.

References.

1. Wiberg E, Wiberg N (2001) *Inorganic Chemistry*. (Academic Press).
2. Herron JT, Huie RE (1980) Rate Constants at 298 K for the Reactions SO+SO+M→(SO)2+M and SO+(SO)2→SO2+S2O. *Chem. Phys. Lett.* 76(2):322–324.
3. Gottlieb CA, Gottlieb EW, Litvak MM, Ball JA, Penfield H (1978) Observations of Interstellar Sulfur Monoxide. *The Astrophysical Journal* 219:77–94.
4. Sakai N, et al. (2014) Change in the Chemical Composition of Infalling Gas Forming a Disk around a Protostar. *Nature* 507(7490):78–80.
5. Na CY, Esposito LW, Skinner TE (1990) International Ultraviolet Explorer Observation of Venus SO2 and SO. *J. Geophys. Res.* 95(D6):7485–7491.
6. Russell CT, Kivelson MG (2000) Detection of SO in Io's Exosphere. *Science* 287(5460):1998–1999.
7. Boissier J, et al. (2007) Interferometric Imaging of the Sulfur-Bearing Molecules H2S, SO, and CS in Comet C/1995 O1 (Hale-Bopp). *Astron. Astrophys.* 475(3):1131–1144.
8. Evolution NRCUCoPB, Chemical (1990) *The Cosmic History of the Biogenic Elements and Compounds*. (National Academies Press (US)).
9. Piro NA, Figueroa JS, McKellar JT, Cummins CC (2006) Triple-Bond Reactivity of Diphosphorus Molecules. *Science* 313(5791):1276–1279.
10. Velian A, et al. (2014) A Retro Diels–Alder Route to Diphosphorus Chemistry: Molecular Precursor Synthesis, Kinetics of P2 Transfer to 1,3-Dienes, and Detection of P2 by Molecular Beam Mass Spectrometry. *J. Am. Chem. Soc.* 136(39):13586–13589.
11. Velian A, Cummins CC (2015) Synthesis and characterization of P2N3 -: An Aromatic Ion Composed of Phosphorus and Nitrogen. *Science* 348(6238):1001–1004.
12. Spinney HA, Piro NA, Cummins CC (2009) Triple-Bond Reactivity of an AsP Complex Intermediate: Synthesis Stemming from Molecular Arsenic, As4. *J. Am. Chem. Soc.* 131(44):16233–16243.
13. Transue WJ, et al. (2016) A Molecular Precursor to Phosphaethyne and Its Application in Synthesis of the Aromatic 1,2,3,4-Phosphatriazolate Anion. *J. Am. Chem. Soc.* 138(21):6731–6734.
14. Velian A, Cummins CC (2012) Facile Synthesis of Dibenzo-7λ3-phosphanorbornadiene Derivatives Using Magnesium Anthracene. *J. Am. Chem. Soc.* 134(34):13978–13981.
15. Transue WJ, et al. (2017) On the Mechanism and Scope of Phosphinidene Transfer from Dibenzo-7-Phosphanorbornadiene Compounds. *J. Am. Chem. Soc.* 139(31):10822–10831.
16. Velian A, Transue WJ, Cummins CC (2015) Synthesis, Characterization, and Thermolysis of Dibenzo-7-dimethylgermanorbornadiene. *Organometallics* 34(19):4644–4646.
17. Hartzell GE, Paige JN (1966) Ethylene Episulfoxide. *J. Am. Chem. Soc.* 88(11):2616–2617.
18. Dodson RM, Sauers RF (1967) Sulphur Monoxide: Reaction with Dienes. *Chem. Commun.* (22):1189–1190.
19. Abu-Yousef IA, Harpp DN (1995) A Useful Precursor for Sulfur Monoxide Transfer. *Tetrahedron Lett.* 36(2):201–204.
20. Abu-Yousef IA, Harpp DN (1997) Effective Precursors for Sulfur Monoxide Formation. *J. Org. Chem.* 62(24):8366–8371.
21. Chow YL, Tam JNS, Blier JE, Szmant HH (1970) Mechanism of Sulphur Monoxide Extrusion. *J. Chem. Soc. D* (23):1604–1605.
22. Grainger RS, Procopio A, Steed JW (2001) A Novel Recyclable Sulfur Monoxide Transfer Reagent. *Org. Lett.* 3(22):3565–3568.
23. Grainger RS, Patel B, Kariuki BM, Male L, Spencer N (2011) Sulfur Monoxide Transfer from peri-Substituted Trisulfide-2-oxides to Dienes: Substituent Effects, Mechanistic Studies and Application in Thiophene Synthesis. *J. Am. Chem. Soc.* 133(15):5843–5852.
24. Nakayama J, Tajima Y, Xue-hua P, Sugihara Y (2007) [1 + 2] Cycloadditions of Sulfur Monoxide (SO) to Alkenes and Alkynes and [1 + 4] Cycloadditions to Dienes (Polyenes). Generation and Reactions of Singlet SO? *J. Am. Chem. Soc.* 129(23):7250–7251.
25. Longobardi LE, Wolter V, Stephan DW (2015) Frustrated Lewis Pair Activation of an N-Sulfinylamine: A Source of Sulfur Monoxide. *Angew. Chem. Int. Ed.* 54(3):809–812.
26. Corey EJ, Mock WL (1962) Chemistry of Diimide. III. Hydrogen Transfer to Multiple Bonds by Dissociation of the Diimide-Anthracene Adduct, Anthracene-9,10-Biimine. *J. Am. Chem. Soc.* 84(4):685–686.
27. Wasserman HH, Scheffer JR (1967) Singlet Oxygen Reactions from Photoperoxides. *J. Am. Chem. Soc.* 89(12):3073–3075.
28. Baldwin JE, Lopez RCG (1982) The Generation and Trapping of Thiobenzaldehyde and Thioacetaldehyde. *J. Chem. Soc., Chem. Commun.* (18):1029–1030.
29. Appler H, Gross LW, Mayer B, Neumann WP (1985) Die Chemie der schweren Carben-Analogen R2M, M = Si, Ge, Sn. *J. Organomet. Chem.* 291(1):9–23.
30. Carpino LA, et al. (1988) Synthesis, Characterization, and Thermolysis of 7-Amino-7-azabenzonorbornadienes. *J. Org. Chem.* 53(11):2565–2572.
31. Courtemanche MA, Transue WJ, Cummins CC (2016) Phosphinidene Reactivity of a Transient Vanadium P≡N Complex. *J. Am. Chem. Soc.* 138(50):16220–16223.

32. Sanz ME, McCarthy MC, Thaddeus P (2003) Rotational Transitions of SO, SiO, and SiS Excited by a Discharge in a Supersonic Molecular Beam: Vibrational Temperatures, Dunham Coefficients, Born–Oppenheimer Breakdown, and Hyperfine Structure. *J. Chem. Phys.* 119(22):11715–11727.
33. Saito S (1969) Detection of Sulfur Monoxide in the Pyrolysis of Ethylene Episulfoxide by Microwave Spectroscopy. *Bull. Chem. Soc. Jpn.* 42(3):667–670.
34. Michaelis A (1889) Über anorganische Derivate des Phenylhydrazins. *Ber. Dtsch. Chem. Ges.* 22(2):2228–2233.
35. Gieren A, Dederer B (1977) X-Ray Structure Analysis of N-Phenyl-N′-sulfinyl-hydrazine. *Angew. Chem. Int. Ed.* 16(3):179–180.
36. Cerioni G, Piras P, Marongiu G, Macciantelli D, Lunazzi L (1981) Conformational Studies by Dynamic Nuclear Magnetic Resonance Spectroscopy. Part 21. Structure, Conformation, and Stereodynamics of Sulphinylhydrazines. *J. Chem. Soc., Perkin Trans. 2* (11):1449–1453.
37. Schanda F, Gieren A, Filhol A (1984) Refinement of the Structure of N-Phenyl-N'-Sulfinylhydrazine, C6H6N2OS, at 120(1) K with Neutron Data. *Acta Crystallogr., Sect. C: Cryst. Struct. Commun.* 40(2):306–308.
38. Nakayama J, et al. (2004) Reversible Disulfur Monoxide (S2O)-Forming Retro-Diels-Alder Reaction. Disproportionation of S2O to Trithio-Ozone (S3) and Sulfur Dioxide (SO2) and Reactivities of S2O and S3. *J. Am. Chem. Soc.* 126(29):9085–9093.
39. Meschi DJ, Myers RJ (1956) Disulfur Monoxide. I. Its Identification as the Major Constituent in Schenk's "Sulfur Monoxide". *J. Am. Chem. Soc.* 78(24):6220–6223.
40. Amano T, Hirota E, Morino Y (1967) Microwave Spectrum of the SO Radical. Equilibrium S-O Distance, Electric Quadrupole Coupling Constant and Magnetic Hyperfine Structure Constants. *J. Phys. Soc. Jpn.* 22(2):399–412.
41. Clark WW, De Lucia FC (1976) The Microwave Spectrum and Rotational Structure of the 1Δ and 3Σ Electronic States of Sulfur Monoxide. *J. Mol. Spectrosc.* 60(1):332–342.
42. Patterson D, Rasmussen J, Doyle JM (2009) Intense Atomic and Molecular Beams via Neon Buffer-Gas Cooling. *New J. Phys.* 11(5):055018.
43. Thorwirth S, et al. (2006) Rotational Spectroscopy of S2O: Vibrational Satellites, 33S Isotopomers, and the Sub-Millimeter-Wave Spectrum. *J. Mol. Struct.* 795(1):219–229.
44. Ellenbroek AW, Dymanus A (1976) Zeeman Effect in SO2 by Beam Maser Zeeman Spectroscopy. *Chem. Phys. Lett.* 42(2):303–306.
45. Colin R (1968) The $b1\Sigma+$–$X3\Sigma-$ Band System of SO. *Can. J. Phys.* 46(13):1539–1546.
46. Müller HSP, Schlöder F, Stutzki J, Winnewisser G (2005) The Cologne Database for Molecular Spectroscopy, CDMS: A useful tool for astronomers and spectroscopists. *J. Mol. Struct.* 742(1):215–227.
47. Wildt J, Fink EH, Winter R, Zabel F (1983) Radiative Lifetime and Quenching of SO($b1\Sigma+,\upsilon'$ = 0). *Chem. Phys.* 80(1):167–175.
48. Klotz R, Marian CM, Peyerimhoff SD, Hess BA, Buenker RJ (1984) Calculation of Spin-Forbidden Radiative Transitions Using Correlated Wavefunctions: Lifetimes of $b1\Sigma+$, $a1\Delta$ States in O2, S2 and SO. *Chem. Phys.* 89(2):223–236.
49. Martin-Drumel MA, McCarthy MC, Patterson D, McGuire BA, Crabtree KN (2016) Automated Microwave Double Resonance Spectroscopy: A Tool to Identify and Characterize Chemical Compounds. *J. Chem. Phys.* 144(12):124202.
50. Andrews L, Hassanzadeh P, Brabson GD, Citra A (1996) Reactions of Nitric Oxide with Sulfur Species. Infrared Spectra and Density Functional Theory Calculations for SNO, SNO+, SSNO, and SNNO in Solid Argon. *J. Phys. Chem.* 100(20):8273–8279.
51. Herges R (2015) Coarctate and Pseudocoarctate Reactions: Stereochemical Rules. *J. Org. Chem.* 80(23):11869–11876.
52. Schenk WA, Leißner J (1987) Freisetzung von Schwefelmonoxid aus seinen Komplexverbindungen [1]. *Z. Naturforsch., B: Chem. Sci.* 42(6):799–800.
53. Chao P, Lemal DM (1973) Sulfur Monoxide Chemistry. Stereochemistry of the Thiirane Oxide-Diene Reaction. *J. Am. Chem. Soc.* 95(3):920–922.
54. Heyke O, Neher A, Lorenz IP (1992) Bis(triphenylphosphan)Palladium-Komplexe mit Schwefeloxid-Liganden. *Z. anorg. allg. Chem.* 608(2):23–27.
55. Schenk WA, Karl U (1989) Chirale Ruthenium-Halbsandwichkomplexe des Schwefelmonoxids und Schwefeldioxids. *Z. Naturforsch., B: Chem. Sci.* 44:988–989.
56. Schenk WA (2011) The Coordination Chemistry of Small Sulfur-Containing Molecules: A Personal Perspective. *Dalton Trans.* 40(6):1209–1219.
57. Bonomo L, Solari E, Scopelliti R, Floriani C (2001) Ruthenium Nitrides: Redox Chemistry and Photolability of the Ru–Nitrido Group. *Angew. Chem. Int. Ed.* 40(13):2529–2531.
58. Leung WH, et al. (2000) Ruthenium Complexes with N(SPR2)2- (R = Ph or Pri). *J. Chem. Soc., Dalton Trans.* 0(3):423–430.
59. Schenk WA, Leissner J, Burschka C (1984) Stabilization of Sulfur Monoxide by Coordination to Transition Metals. *Angew. Chem. Int. Ed.* 23(10):806–807.

An Anthracene-based Molecular Precursor for Sulfur Monoxide Delivery: Thermal Release, Spectroscopic Identification and Transfer Reactivity

Maximilian Joost, Matthew Nava, Wesley J. Transue, Marie-Aline Martin-Drumel, David Patterson, Christopher C. Cummins*

Supporting Information

Table of Contents

S.1 Experimental Details and Characterization of Products **S.3**

S.1.1 General Information S.3

S.1.2 Synthesis of **1** S.4

S.1.3 Thermal Decomposition of **1** S.6

S.1.4 Reaction of **1** With 3,5-Di-*tert*-butyl-1,2-quinone S.12

S.1.5 Reaction of **1** With 2,3-Dimethyl-1,3-butadiene S.12

S.1.6 Reaction of **1** With 1,3-Cyclohexadiene S.12

S.1.7 Reaction of **1** With Norbornadiene S.13

S.1.8 Synthesis of [RuCl(Cp*)(SO)(PCy_3)] S.13

S.1.9 Synthesis of **2** S.13

S.2 Microwave Spectroscopy Studies of the Gases Evolved from 1 **S.16**

S.2.1 Prenozzle Thermolysis Studies S.16

S.2.2 Buffer-gas Cell Studies S.18

S.3 Assignment of the Microwave Spectrum of 1 **S.19**

S.3.1 Analysis S.19

S.3.2 Spectroscopic Constants Determination S.23
S.3.3 Structure of **1** S.25
S.3.4 General Remarks and Consequences S.25

S.4 X-Ray Diffraction Studies **S.26**
S.4.1 Data acquisition S.26

S.5 Computational Details **S.28**
S.5.1 Comparison of Precursor Thermodynamics S.28
S.5.2 Mechanistic Investigation of the Fragmentation of **1** S.28
S.5.3 Nudged Elastic Band Calculations S.28

S.6 Construction and Use of a Gas-IR cell **S.30**

References **S.33**

S.1 Experimental Details and Characterization of Products

S.1.1 General Information

The synthesis and workup of OSN_2**A** (7-sulfinylamino-2,3:5,6-dibenzo-7-azabicyclo[2.2.1]hepta-2,5-diene, **1**, **A** = 9,10-dihydroanthracene-9,10-diyl) was performed under air employing ACS reagent grade solvents. All other manipulations were performed in a Vacuum Atmospheres model MO-40M glovebox under an inert atmosphere of purified N_2. All solvents were obtained anhydrous and oxygen-free by bubble degassing (Ar), purification through columns of alumina and Q5,[1] and storage over molecular sieves.[2] Deuterated solvents were purchased from Cambridge Isotope Labs, then degassed and stored over molecular sieves for at least 2 days prior to use. Celite 435 (EM Science) and activated charcoal were dried by heating above 250 °C under dynamic vacuum for at least 48 h prior to use. Glassware was oven-dried for at least three hours at temperatures greater than 150 °C. 7-Amino-2,3:5,6-dibenzo-7-azabicyclo[2.2.1]hepta-2,5-diene (H_2N_2**A**) was prepared as previously described by Carpino and coworkers.[3] [RuCl(Cp*)(PCy_3)] (Cp* = η^5-$C_5Me_5^-$) was prepared as described by Tilley and coworkers.[4] $[Na(DME)_3]_2[Ru(N_4Me_8)]$ (N_4Me_8) = *meso*-octamethylporphyrinogen) was prepared as described by Floriani and coworkers.[5] Yields for the reaction of **1** with organic substrates were determined by ^{1}H NMR spectroscopy. NMR spectra were obtained on Varian Inova 300 and 500 instruments equipped with Oxford Instruments superconducting magnets, on a Jeol ECZ-500 instrument equipped with an Oxford Instruments superconducting magnet, or on a Bruker Avance 400 instrument equipped with a Magnex Scientific or with a SpectroSpin superconducting magnet. ^{1}H NMR and ^{13}C NMR spectra were referenced internally to residual solvent signals,[6] and ^{31}P NMR spectra were referenced externally to 85% aq. H_3PO_4. Variable temperature NMR measurements were calibrated with a methanol or ethylene glycol thermometer.[7]

Attenuated total reflection infrared (ATR-IR) and gas-phase IR spectra (see S.6) were recorded on a Bruker Tensor 37 Fourier transform IR (FTIR) spectrometer.

Absorption spectral measurements were performed using an Ocean Optics USB4000 spectrophotometer with a DT-Mini-2GS UV-vis-NIR light source and a Qblue heating block. Quartz cells (sealable with a teflon-lined screw cap) with a path length of 1 cm were used.

Elemental analyses were performed by Robertson Microlit Laboratories (Ledgewood, NJ, USA).

S.1.2 Synthesis of 1

A solution of H_2N_2**A** (200.0 mg, 0.96 mmol, 1.0 equiv) in dry Et_2O (30 mL) was transferred into a Schlenk flask under nitrogen. Et_3N (268 µL, 1.92 mmol, 2.0 equiv) was added using a microsyringe and the suspension was cooled by means of an icebath. A solution of thionyl chloride (70 µL, 0.96 mmol, 1.0 equiv) in dry Et_2O (10 mL) was added dropwise using a syringe at 0 °C to the suspension over ca. 10 min. Upon addition, a thick, colorless precipitate formed. The mixture was stirred for 3 h while slowly warming up to ambient temperature. The precipitate was removed by filtration, washed with Et_2O (ca. 50 mL) and all volatile materials of the combined filtrate were removed under vacuum to yield pure **1** as a colorless solid. Yield: 203.0 mg (0.80 mmol, 83 %. Crystals suitable for an X-ray diffraction analysis were grown from a concentrated solution of **1** in Et_2O at −30 °C.

Elem. Anal. Found(Calc'd) for $C_{14}H_{10}N_2OS$: C 66.24 (66.12), H 3.94 (3.96), N 10.96 (11.02). ^{1}H NMR (chloroform-*d*, 500 MHz, 20 °C) δ 7.41 (m, 4H, H_{ar}), 7.09 (m, 4H, H_{ar}), 6.36 (s, 2H, $H_{bridgehead}$); $^{13}C\{^1H\}$ NMR (chloroform-*d*, 126 MHz, 20 °C): δ 145.1 (s, C_{ipso}), 126.6 (s, CH_{ar}), 122.3 (s, CH_{ar}), 74.4 (s, $CH_{bridgehead}$); IR (ATR): 1179 cm^{-1}, 1087 cm^{-1} (antisym. and sym. NSO stretch vibration, respectively).

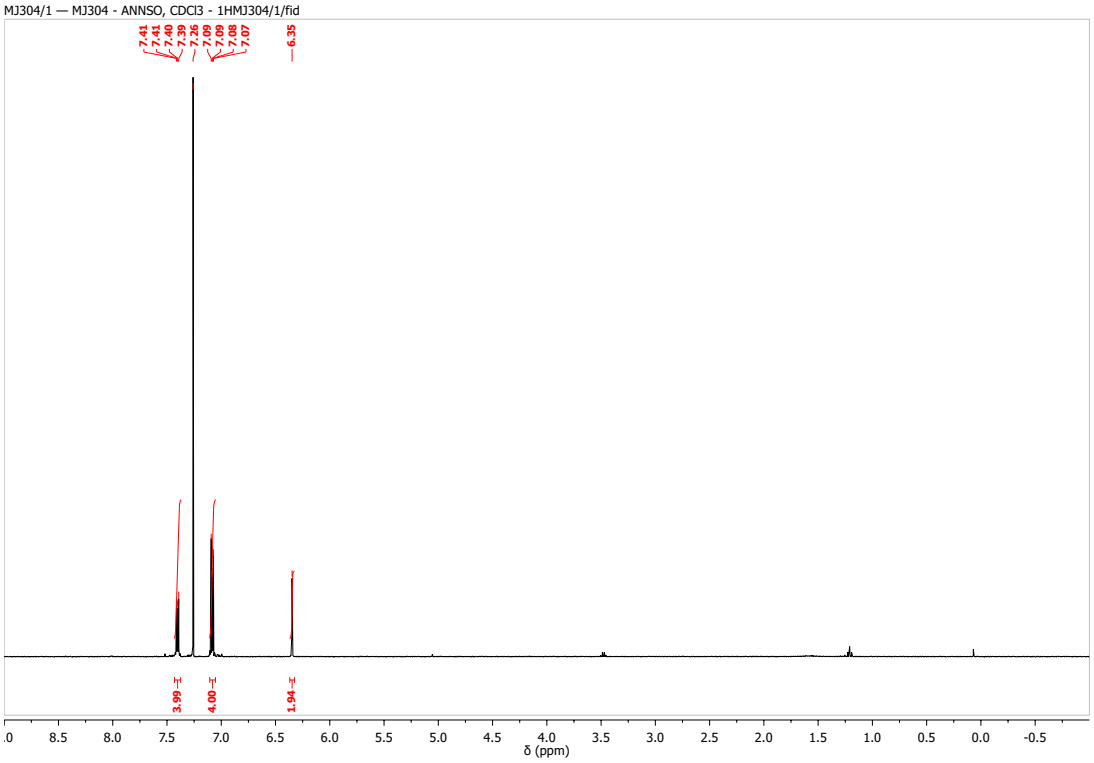

Figure S.1: ^{1}H NMR spectrum (chloroform-*d*, 500 MHz, 20 °C) of **1**.

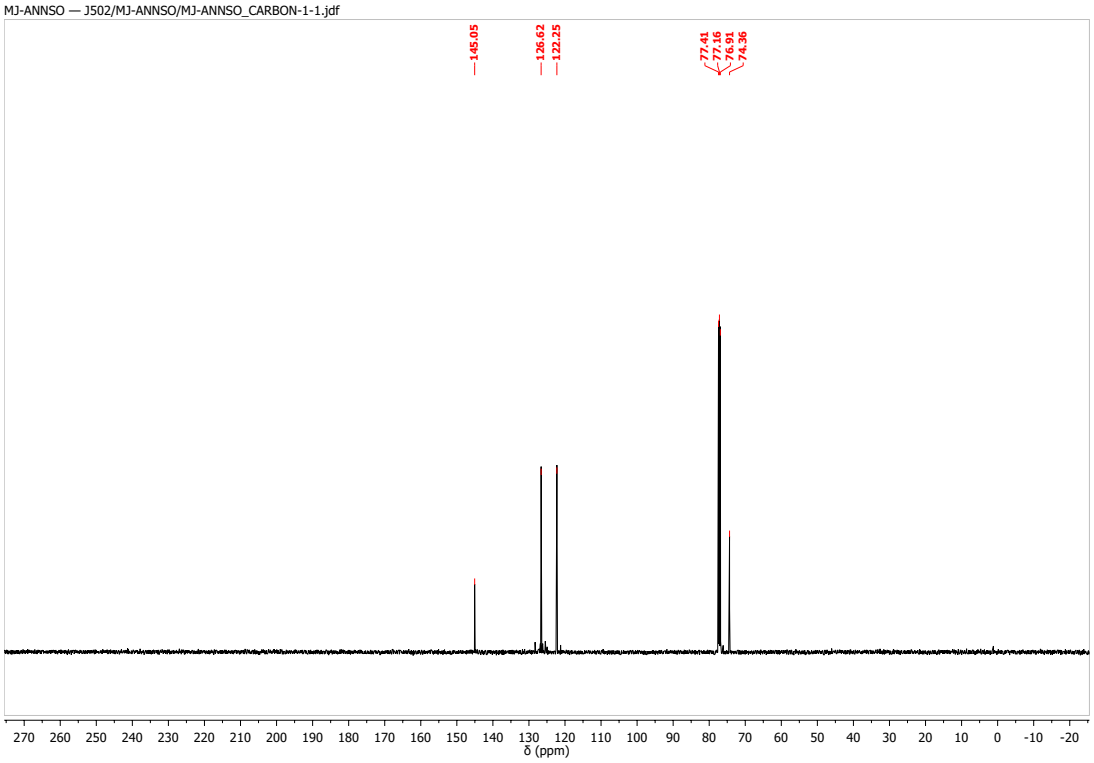

Figure S.2: ^{13}C{^{1}H} NMR spectrum (chloroform-*d*, 126 MHz, 20 °C) of **1**.

S.1.3 Thermal Decomposition of 1

The thermal decomposition of **1** was studied in the solid state and in solution:

S.1.3.1 Thermogravimetric Analysis

The platinum pan of a TGA Q500 V20.10 Build 36 instrument was charged with **1** (ca. 3 mg). The temperature was slowly increased to 400 °C at a rate of 3 °C min^{-1} using N_2 as the carrier gas.

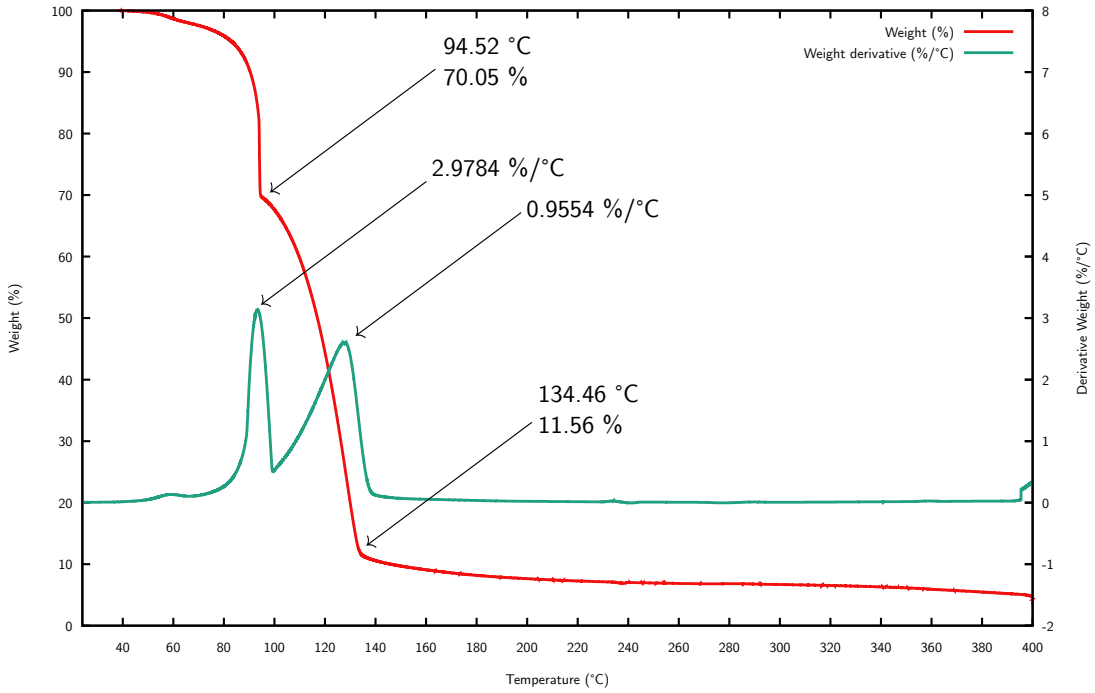

Figure S.3: Thermogravimetric analysis of **1**.

S.1.3.2 IR Spectroscopy

A gas-IR cell (see section S.6) was used to analyze the gases evolved upon thermolysis of **1**. A gas-IR cell featuring a sample pocket was charged with ca. 5 mg of **1** and evacuated (oil pump vacuum). After recording a blank spectrum of the cell, the sample pocket was heated using a heat gun, leading to decomposition of **1**, and an IR spectrum was subsequently acquired (Figure S.4). SO_2 was identified as the major component in the spectrum by comparison with reported data.[8,9]

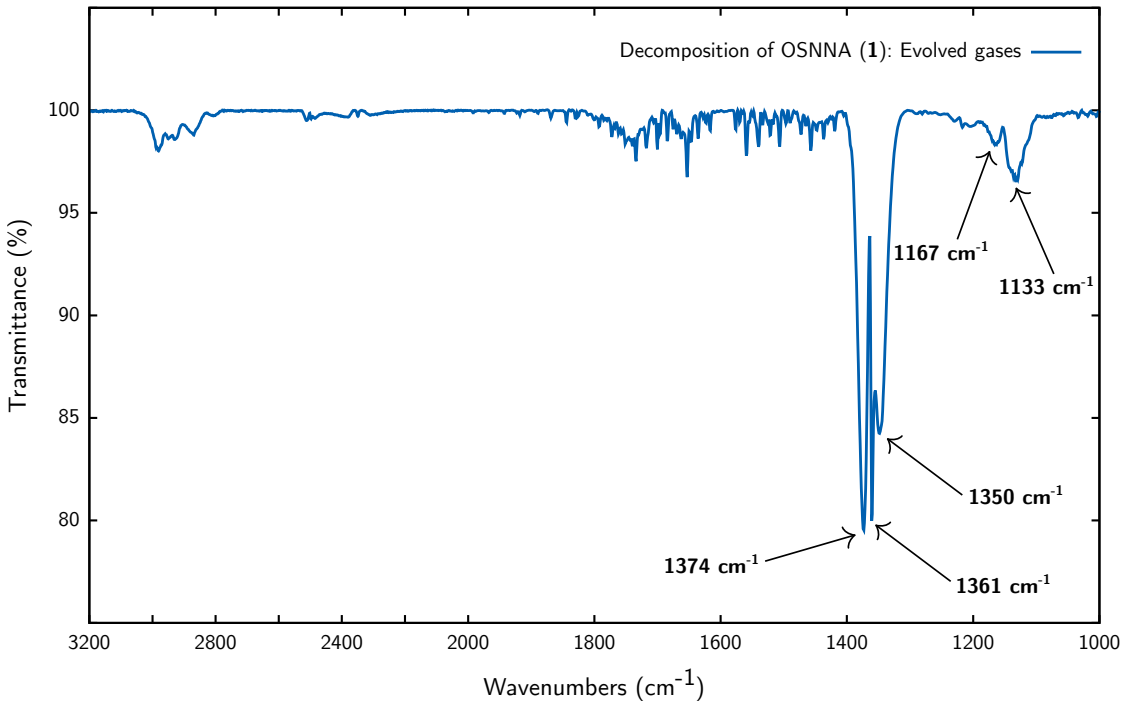

Figure S.4: IR-spectrum of the gases evolved upon thermolysis of **1**. The bands centered around 1360 cm^{-1} and 1150 cm^{-1} correspond to the the asymmetric and symmetric stretching modes of SO_2, respectively.

S.1.3.3 MBMS Analysis

The molecular beam mass spectrometer (MBMS) apparatus has been previously described.[10] Briefly, the apparatus consists of two high vacuum chambers designated the source and detection chamber. The source chamber consists of a sample holder suspended in the middle of the vacuum chamber. The sample holder is a hollow stainless steel cylinder directed at a 1 mm diameter skimmer from the source chamber to the detection chamber. The stainless steel cup is loaded with 10 to 15 mg of sample, restrained with a cap and a stainless steel screen (98% open area, Unique Wire Weaving Co), resistively heated with cartridge heater (Comstat Inc) inserted in a copper bar brazed onto the stainless steel sample cylinder and the temperature is monitored with a type K thermocouple reader bolted onto the copper bar. The sample was heated with a manual temperature ramp and the temperature was recorded using a National Instruments temperature logger with data points being recorded every 3 seconds. Once gases are evolved from the sample, they pass unimpeded through a 1 mm diameter skimmer from the source chamber to the detection chamber, creating a molecular beam. The molecular beam is then sent to the entrance of an axially oriented Extrel MAX500 Mass Spectrometer (Extrel Core Mass Spectrometers), where the beam is ionized by EI (70 eV),

mass separated by a quadrupole and detected by a Faraday cup. The masses of interest are monitored as a function of temperature and are baseline corrected for background signal. Masses from 20-300 m/z were recorded. A moving average of 7 scans was used to smooth out the data.

S.1.3.4 Decomposition in Solution

a) ^{1}H NMR spectroscopic analysis:

A solution of **1** (10.0 mg, 0.04 mmol) and hexamethylbenzene in benzene-d_6 (c = 1.51 g mL^{-1}, 0.7 mL) was transferred into an NMR tube. The tube was sealed and introduced within 10 min into an NMR spectrometer with a probe preheated to 80 °C. After thermal equilibration (10 min), locking and shimming, ^{1}H NMR spectra were recorded at fixed intervals (1 min) over the course of 3.5 h.

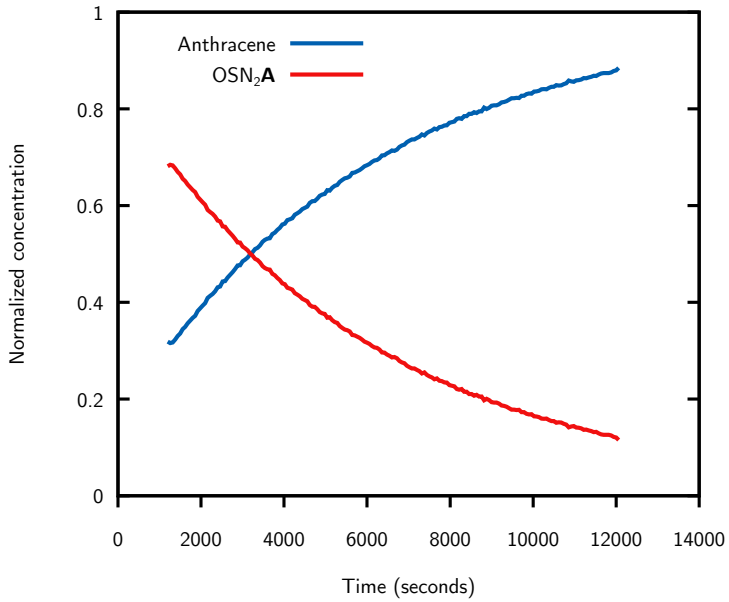

Figure S.5: Thermal decay of **1** at 80 °C in benzene-d_6: Plot of the concentrations of **1** and **A** over time.

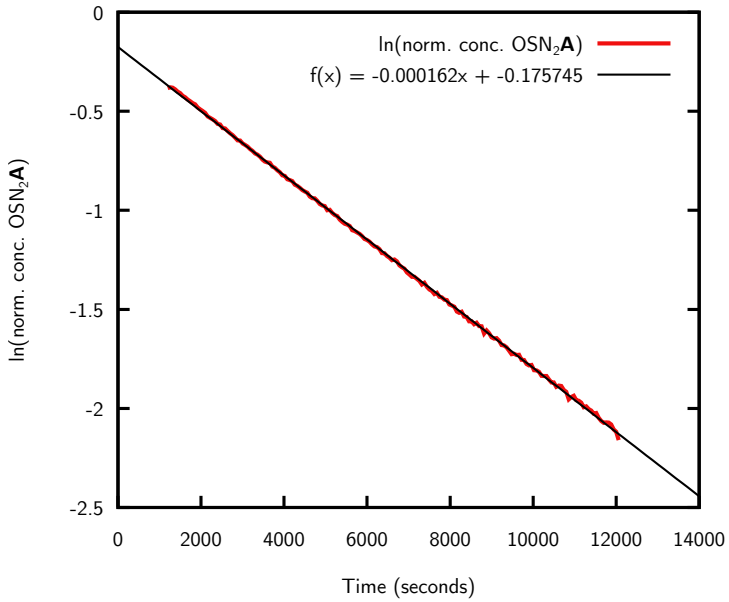

Figure S.6: Thermal decay of **1** at 80 °C in benzene-d_6: Plot of the the natural logarithm of the concentration of **1** over time, indicating a linear relationship and thus first-order behavior.

b) UV-Vis spectroscopic analysis:

A solution of **1** (0.1 mM, 3 mL in dry THF) was transferred at 25 °C into a quartz cuvette. A small stirbar was added, the cuvette closed with a screwcap and introduced into the spectrophotometer preheated at 80 °C. After equilibration (3 min), spectra were recorded with magnetical stirring (500 rpm) every 2 min to 5 min for 3 to 4 hours. A total of 4 runs was recorded. For every run, a blank spectrum for background correction was recorded prior to the experiment at 80 °C using neat THF after thermal equilibration (5 min).

For data analysis, only the disappearance of **1** (at 289 nm) was analyzed. Anthracene formation cannot easily followed due to overlapping bands.

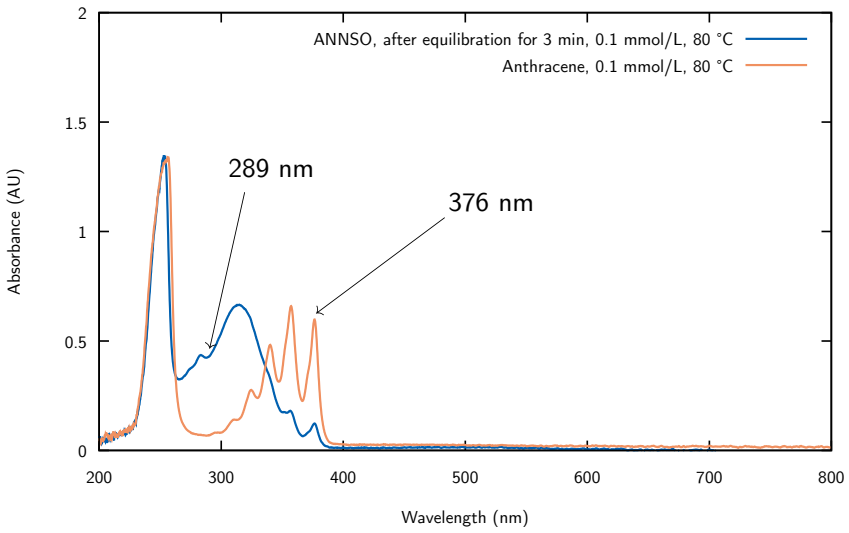

Figure S.7: UV-Vis spectra of **1** (blue) and **A** (orange) in THF (0.1 mM) at 80 °C.

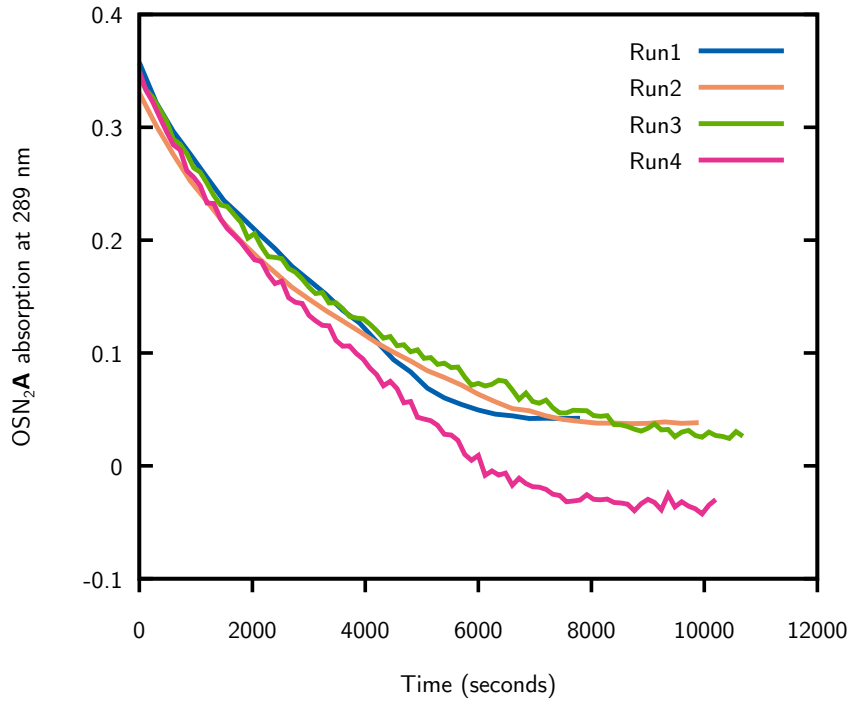

Figure S.8: Thermal decay of **1** at 80 °C in THF: Plot of the absorption of **1** at 289 nm over time.

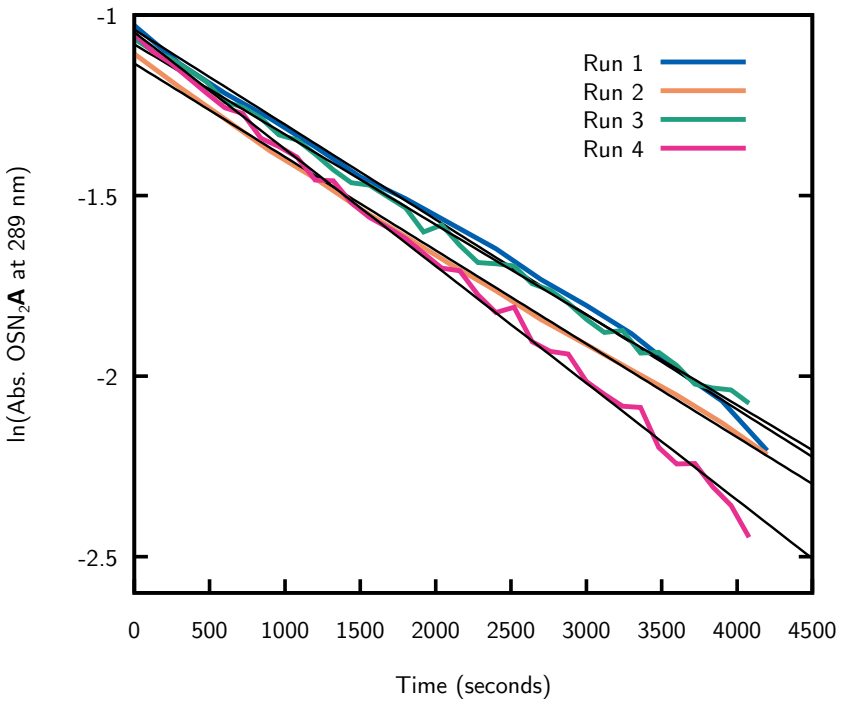

Figure S.9: Thermal decay of **1** at 80 °C in THF: Plot of the the natural logarithm of the absorption of **1** at 289 nm over time. The equations corresponding to the linear regression lines are summarized in Table S.1.

Table S.1: Determination of k_{obs} for the thermolysis of **1** at 80 °C in THF.

Run	Linear fit	k_{obs} (s^{-1})
1	$f(x) = -0.0002631x - 1.0405291$	$2.631 \cdot 10^{-4}$
2	$f(x) = -0.0002592x - 1.1342832$	$2.592 \cdot 10^{-4}$
3	$f(x) = -0.0002503x - 1.0811323$	$2.503 \cdot 10^{-4}$
4	$f(x) = -0.0003244x - 1.0474914$	$3.244 \cdot 10^{-4}$
avg		$(2.743 \pm 0.436) \cdot 10^{-4}$

S.1.4 Reaction of 1 With 3,5-Di-*tert*-butyl-1,2-quinone

A solution of 3,5-di-*tert*-butyl-1,2-benzoquinone (8.6 mg, 0.04 mmol, 1.0 equiv) in benzene-d_6 (0.4 mL) was added to a solution of **1** (10.0 mg, 0.04 mmol, 1.0 equiv) in benzene-d_6 (0.4 mL) at 25 °C. The dark green mixture was transferred to an NMR tube and heated for 24 h at 70 °C. During this time, the dark green color faded slowly to light green, then yellow. Analysis by ^{1}H NMR spectroscopy revealed quantitative conversion to the corresponding phenyl sulfite (4,6-di-*tert*-butylbenzo[*d*][1,3,2]dioxathiole 2-oxide). This compound was previously prepared and characterized.[11,12]

^{1}H NMR (benzene-d_6, 400 MHz, 20 °C) δ 7.10 (d, $^4J_{HH}$ = 2.0 Hz, 1H, $H_{ar\text{-}4}$), 6.91 (d, $^4J_{HH}$ = 2.0 Hz, 1H, $H_{ar\text{-}6}$), 1.31 (s, 9H, H_{CH_3}), 1.21 (s, 9H, H_{CH_3}); ^{13}C{^{1}H} NMR (benzene-d_6, 126 MHz, 20 °C): δ 147.9 (s, C_5), 143.5 (s, C_2), 138.9 (s, C_3), 135.7 (s, C_1), 118.5 (s, C_4), 108.0 (s, C_6); 35.0 (s, $C(CH_3)_3$), 34.7 (s, $C(CH_3)_3$), 31.5 (s, $C(CH_3)_3$), 29.6 (s, $C(CH_3)_3$); MS (EI, 70 eV) m/z 268.

S.1.5 Reaction of 1 With 2,3-Dimethyl-1,3-butadiene

2,3-Dimethyl-1,3-butadiene (0.6 mL) was added to **1** (10.0 mg, 0.04 mmol, 1.0 equiv) in an NMR tube. The tube was sealed and heated for 16 h to 80 °C. The mixture was allowed to cool to ambient temperature, all volatile materials were removed under vacuum, and the residue was dissolved in chloroform-*d*. ^{1}H NMR spectroscopic analysis indicated complete conversion of the sulfonylhydrazine and formation of the previously reported 3,4-dimethyl-2,5-dihydrothiophene 1-oxide. Yield: 60%.[13]

^{1}H NMR (chloroform-*d*, 400 MHz, 20 °C) δ 3.82 (md, $^2J_{HH}$ = 17.3 Hz, 2H, H_{SCH}), 3.45 (md, $^2J_{HH}$ = 17.3 Hz, 2H, H_{SCH}), 1.78 (s, 6H, H_{CH_3}).

S.1.6 Reaction of 1 With 1,3-Cyclohexadiene

1,3-Cyclohexadiene (19 µL, 0.20 mmol, 5.0 equiv) was added to a solution of **1** (10.0 mg, 0.04 mmol, 1.0 equiv) in C_6D_6 (0.8 mL) in an NMR tube. After 24 h of heating in an oilbath at 70 °C, ^{1}H NMR spectroscopic analysis indicated complete conversion of the sulfonylhydrazine and formation of the previously reported 7-thianorbornadiene S-oxide. Yield: 59%.[14]

^{1}H NMR (benzene-d_6, 400 MHz, 20 °C) δ 5.33 (dd, $^3J_{HH}$ = 3.3 Hz, $^4J_{HH}$ = 2.7 Hz, 2H, $H_{HC=CH}$), 2.94 (m, $^3J_{HH}$ = 3.3 Hz, 2H, $H_{bridgehead}$), 2.28 (m, 2H, H_{CH_2}), 1.03 (m, 2H, H_{CH_2}); ^{1}H NMR (chloroform-*d*, 400 MHz, 20 °C) δ 6.14 (dd, $^3J_{HH}$ = 3.3 Hz, $^4J_{HH}$ = 2.9 Hz, 2H, $H_{HC=CH}$), 3.72 (m, $^3J_{HH}$ = 3.3 Hz, 2H,

$H_{bridgehead}$), 2.44 (m, 2H, H_{CH_2}), 1.66 (m, 2H, H_{CH_2}).

S.1.7 Reaction of 1 With Norbornadiene

Norbornadiene (40 µL, 0.40 mmol, 10 equiv) was added to a solution of **1** (10.0 mg, 0.04 mmol, 1.0 equiv) in $CDCl_3$ (0.7 mL) in an NMR tube. After 16 h at 25 °C, ^{1}H NMR spectroscopic analysis indicated complete conversion of the sulfonylhydrazine and formation of the previously reported norbornadiene-episulfoxide. Yield: 55%.[14]

^{1}H NMR (benzene-d_6, 400 MHz, 20 °C) δ 5.62 (m, 2H, $H_{HC=CH}$), 2.60 (m, 2H, H_{SCH}), 2.44 (m, 2H, $H_{bridgehead}$), 0.24 (m, 2H, H_{CH_2}); ^{1}H NMR (chloroform-d, 400 MHz, 20 °C) δ 6.35 (m, 2H, $H_{HC=CH}$), 3.47 (m, 2H, H_{SCH}), 2.96 (m, 2H, $H_{bridgehead}$), 0.94 (md, $^2J_{HH}$ = 10.0 Hz, 1H, H_{CH_2}), 0.83 (md, $^2J_{HH}$ = 10.0 Hz, 1H, H_{CH_2}).

S.1.8 Synthesis of [RuCl(Cp*)(SO)(PCy_3)]

A colorless solution of **1** (25.0 mg, 0.10 mmol, 1.0 equiv) in THF (4 mL) was added slowly at 25 °C to a blue solution of [RuCl(Cp*)(PCy_3)] (54.3 mg, 0.10 mmol, 1.0 equiv) in THF (4 mL). The mixture was stirred for 30 min at 25 °C. A gradual color change from blue to red-brown was observed. All volatile materials were removed *in vacuo*. The brown residue was dissolved in benzene/pentane (1:1, 3 mL) and filtered through a pad of charcoal (height: 4 cm; in Pasteur pipette). The pad was eluted with a minimal amount of benzene until the filtrate was nearly colorless (ca. 2 mL). All volatile materials were removed under vacuum. The brown residue was washed with pentane (2 mL) and the remaining solid dried under vacuum to give the title compound as a red-brown powder which matches the reported NMR spectroscopic data.[15] Yield: 48.6 mg (0.08 mmol, 82 %).

^{1}H NMR (benzene-d_6, 400 MHz, 20 °C) δ 2.65–1.05 (m, 33H, $H_{cyclohexyl}$), 1.37 (d, $^4J_{HP}$ = 1.0 Hz, 15H, H_{CH_3}); ^{31}P{^{1}H} NMR (benzene-d_6, 162 MHz, 20 °C) δ 40.6 (s, $RuPCy_3$).

S.1.9 Synthesis of 2

THF (2 mL) was added at 25 °C to $[Na(DME)_3]_2[Ru(N_4Me_8)]$ (55.0 mg, 0.050 mmol, 1.0 equiv) and **1** (14.0 mg, 0.055 mmol, 1.1 equiv) placed in a scintillation vial. With rapid stirring, the reaction mixture quickly turned homogeneous and to a dark brown color. After stirring for 60 min, all volatile materials were

removed under reduced pressure to leave a dark orange-brown residue. Repeatedly adding diethyl ether (2 mL), then removal of all volatile materials *in vacuo* removed residual THF. The solids were washed with diethyl ether (3 × 2 mL), and dried under vacuum. Dissolution in THF (1 mL), addition of DME (2 mL), and storage at −35 °C overnight yielded brown microcrystalline solids. After isolation and drying, these solids weighed 23.0 mg (0.025 mmol, 51 %).

This compound is highly sensitive to oxygen and moisture. Several attempts to obtain satisfactory elemental analysis data for **2** were unsuccessful. ^{1}H NMR (THF-d_8, 500 MHz, 20 °C) δ 6.00 (s, 8H, pyrrole CH), 3.40 (s, DME CH_2), 3.23 (s, DME CH_3), 1.61 (s, 12H, pyrrole CH_3), 1.39 (s, 12H, pyrrole CH_3); ^{1}H NMR (DMSO-d_6, 500 MHz, 20 °C) δ 5.77 (s, 8H, pyrrole CH), 3.43 (s, DME CH_2), 3.24 (s, DME CH_3), 1.54 (s, 12H, pyrrole CH_3), 1.28 (s, 12H, pyrrole CH_3); ^{13}C{^{1}H} NMR (DMSO-d_6, 126 MHz, 20 °C): δ 142.7 (s, quaternary pyrrole C), 100.1 (s, pyrrole CH), 71.1 (s, DME CH_2), 58.1 (s, DME CH_3), 38.6 (s, pyrrole CH_3), 38.1 (s, quaternary alkyl C), 30.3 (s, pyrrole CH_3); IR (ATR, under N_2 atmosphere): 1021 cm^{-1} (SO stretching vibration mode).

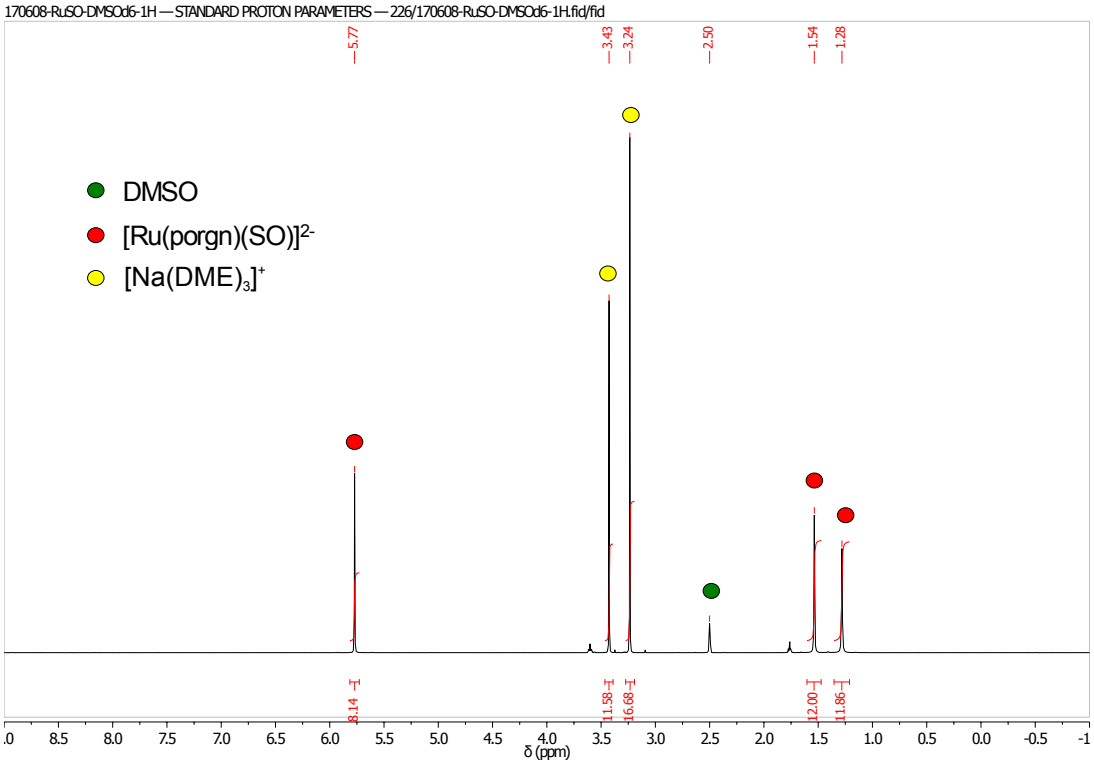

Figure S.10: ^{1}H NMR spectrum (DMSO-d_6, 500 MHz, 20 °C) of **2**.

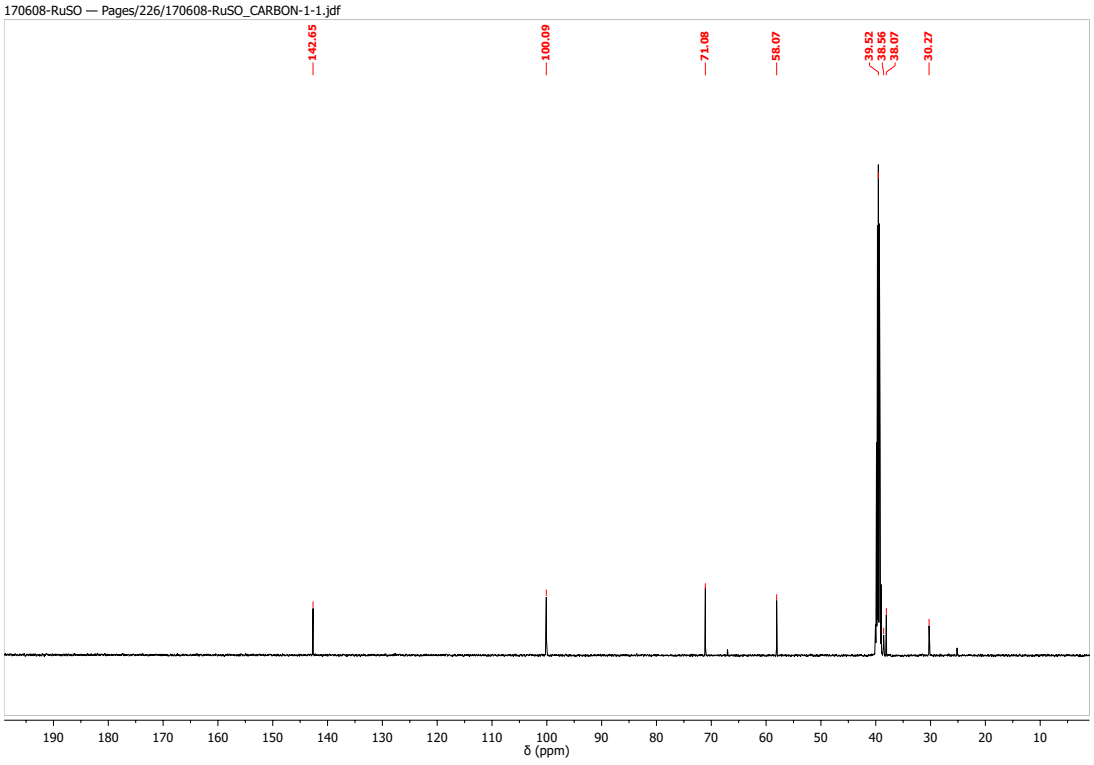

Figure S.11: ^{13}C{^{1}H} NMR spectrum (chloroform-*d*, 126 MHz, 20 °C) of **2**.

S.2 Microwave Spectroscopy Studies of the Gases Evolved from 1

S.2.1 Prenozzle Thermolysis Studies

Preliminary microwave spectroscopic studies of the gases evolved from **1** were undertaken using a prenozzle thermolysis setup. In this setup, a 10 mL stainless steel sample cylinder (SS-4CD-TW-10, Swagelok) loaded with **1** (100 mg) was placed directly behind a general valve (Series 9, Parker Microfluidics). The sample cylinder was wrapped with an ultra-thin heat sheets (35475K443, McMaster-Carr) and a K-type thermocouple was affixed to the heat sheet. The sample cylinder was then heated under neon buffer gas (2.5 kTorr) and expanded into the cavity of a microwave spectrometer with spectral coverage from 5 to 40 GHz.[16,17] The frequencies at which transitions for SO_2 ($1_{1,1} \leftarrow 2_{0,2}$, 12256.589 MHz),[18] S_2O ($2_{1,2} \leftarrow 3_{0,3}$, 17728.909 MHz),[19] S_2O_2 ($1_{1,1} \leftarrow 0_{0,0}$, 15717.946 MHz),[19] $^3\Sigma^-$ SO ($1_2 \leftarrow 1_1$, 13043.7 MHz)[20] and $^1\Delta$ SO (42591.2315 MHz, calculated from rotational constants derived from data reported by Clark and De Lucia)[21] were scanned. Both SO_2 and S_2O, disporportionation products of SO, were present in high intensity (Figures S.12, S.13) but neither electronic state of SO nor its dimer could be detected. This result suggests that the disporportionation of SO is significantly faster than the average residence time of a gaseous molecule evolved from **1** in the current experimental setup. This result then prompted us to investigate the thermolysis of **1** under high vacuum in a buffer-gas cell (*vide infra*).

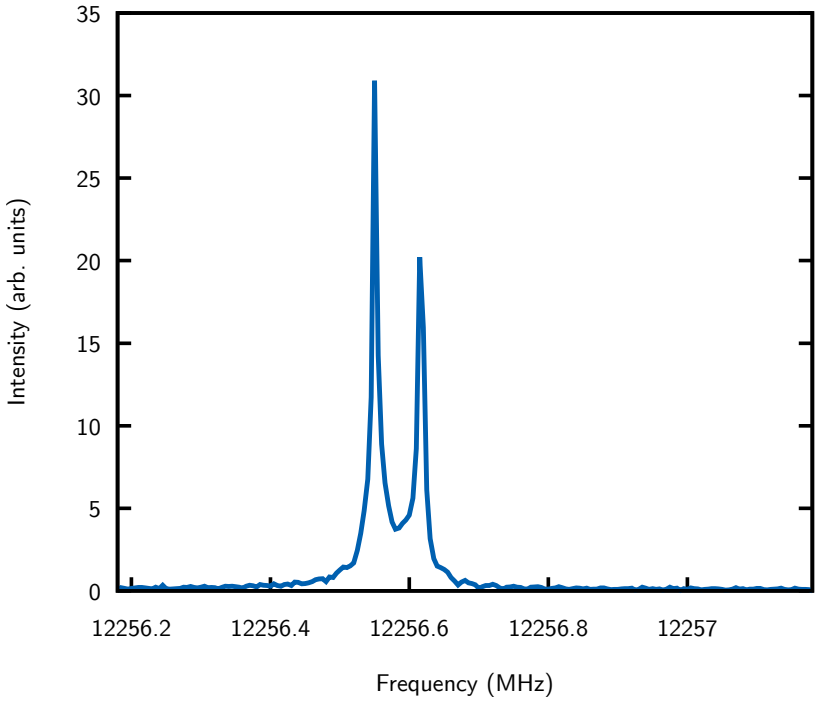

Figure S.12: $1_{1,1} \leftarrow 2_{0,2}$ transition of SO_2 at 12256.589 MHz[18] after thermolysis of a sample of **1** in a cylinder just behind a general valve. The two observable lines are due to Doppler doubling.

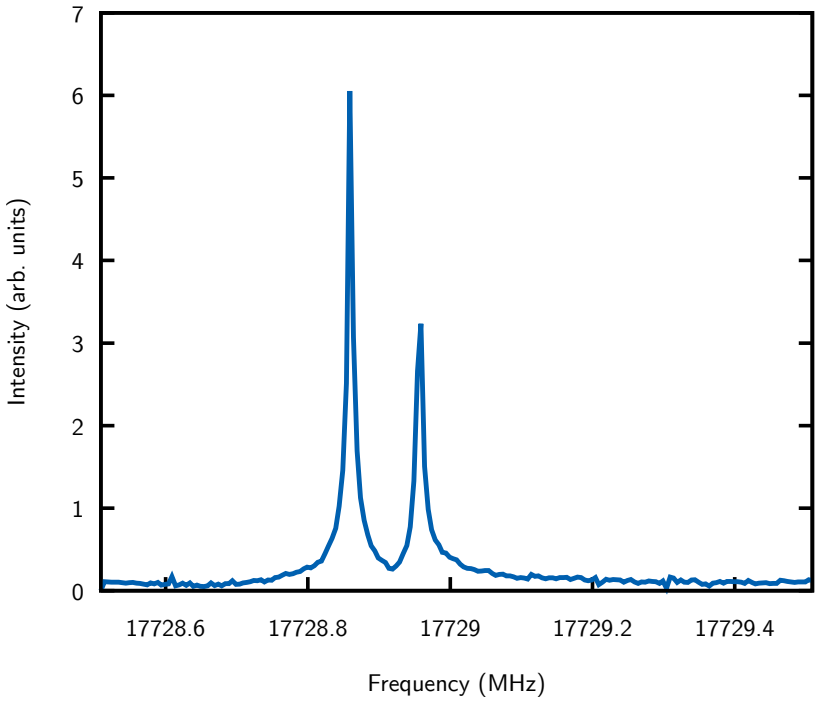

Figure S.13: $2_{1,2} \leftarrow 3_{0,3}$ transition of S_2O at 17728.909 MHz[19] after thermolysis of a sample of **1** in a cylinder just behind a general valve. The two observable lines are due to Doppler doubling.

S.2.2 Buffer-gas Cell Studies

The rotational spectra were taken in a 10 Kelvin buffer gas cell, similar to the one previously described.[22] The cell was made of 101 alloy oxygen free copper. Powder samples were held in a copper crucible in vacuum 1 cm away from a 1.1 cm aperture in a cold cell. 6 standard cubic centimeters/minute of cold helium gas were injected into the cell, from a gas manifold surrounding the input aperture. The sample was heated in the temperature range of 85 °C to 93 °C. The cell is cooled by a closed cycle pulse-tube refrigerator (Cryomech PT415), and is surrounded by an aluminum black-body radiation shield at about 60 K; the sample is held within a small port (2 cm diameter) through this radiation shield.

The electronics are an implementation of chirped-pulse microwave spectroscopy, ideologically similar to the one described by Pate and coworkers.[23] The spectrum is recorded in segments of 85 MHz bandwidth. In each segment, an intermediate frequency (25–110 MHz) chirp from an arbitrary waveform generator (Rigol DG4202) is upconverted by mixing with a microwave frequency local oscillator (Hittite HMCT2200). The upconverted pulse is amplified by a solid state amplifier (Mercury Systems L1218) with a 33 dBm saturated output power, and transmitted into the cold cell via a standard microwave horn (Pasternack enterprises PE5894). Free induction decay signals from the cold molecular sample are detected by a cryogenic low noise amplifier (Low Noise Factory LNF-LNC6-20B, at 6 K, which is protected by a cryogenic high-bandwidth microwave switch (Hittite Microwave, HMC547ALC3), 6 K. The HMC547ALC3 is not rated to perform at temperatures below 233 K, but appears to function to 4 K. The free induction decay is downconverted to 25–110 MHz, further amplified (Stanford Research Systems SRS445), and recorded by a dedicated signal averager (KeySight U1084A). Each segment is recorded for 25 microseconds, including a 4 microsecond chirp and a dead time of about 2 microseconds. The signals are recorded at a sampling rate of 1 GSample/second. The free induction decay shows a characteristic decay time of about 8 microseconds, arising from collisions with the background helium gas, i.e. collisional broadening. The entire excitation/detection sequence is repeated at 40 kHz. An external, non-uniform magnetic field can be applied via a permanent magnet held outside the cryostat. This magnetic field gradient effectively washes out any spectral lines from open-shell species, which exhibit large Zeeman shifts.

S.3 Assignment of the Microwave Spectrum of 1

S.3.1 Analysis

The analysis of the recorded experimental spectrum was challenging to interpret as *ab initio* quantum chemical calculations were not performed on the comparatively large **1**, meaning that its structure in the gas phase, and thus its spectroscopic constants, were initially unknown. To enable a fast analysis of the spectrum, an approach adapted from the AMDOR (for *Automated Microwave DOuble Resonance*) technique developed by some of us.[24] The AMDOR method consists of first identifying transitions sharing an energy level (either upper or lower) on the spectrum, ideally by means of double resonance experiments, and second to use these "linked" transitions to determine the quantum numbers assignment of the energy levels involved in each transition using a "brute force" algorithm that tries all assignment possibilities. In the present version of the AMDOR script, only three quantum numbers (namely J, K_a, K_c) can be assigned to each energy level of the molecule, thus discarding any potential hyperfine structure. A close look at the experimental spectrum revealed several transitions with a partially resolved structure, likely due to nitrogen hyperfine splitting. Considering the limited number of such resolved transitions, we decided to treat **1** as a standard asymmetric top molecule described only with three quantum numbers, and thus to use the central frequency of the partially resolved components in the analysis.

The buffer-gas cell in its current configuration is not able to perform double resonance measurements, which prevented a conventional use of the AMDOR technique. Visual inspection of the spectrum, however, revealed series of transitions equally spaced in frequency, by roughly 555 MHz, as illustrated by Figure S.14. Such a structure is typical of an a-type series of transitions ($\Delta K_a = 0$), as illustrated in Figure S.15. Assuming a-type selection rules ($\Delta J = \pm 1$, $\Delta K_a = 0$, $\Delta K_c = \pm 1$) and knowing that for a given energy level $K_a + K_c = J$ or $J+1$, there are only a limited number or quantum number assignments for each line in each series which can all be tested by the AMDOR algorithm to find the proper assignment. For each possible assignment of the series, the script calls the `spfit` program from H. M. Pickett,[25] which adjusts the three rotational constants A, B, and C. The best assignment is then determined as the one with the smallest standard deviation.

In the first step, the AMDOR algorithm was used on the strongest series in the experimental spectrum, later referred to as series1 (Figure S.14). All quantum number possibilities in the range $10 \leq J \leq 45$ and $0 \leq K_a \leq 10$ (for the first line of the series), thus a number of 665 possibilities, were tested in about 30 s,

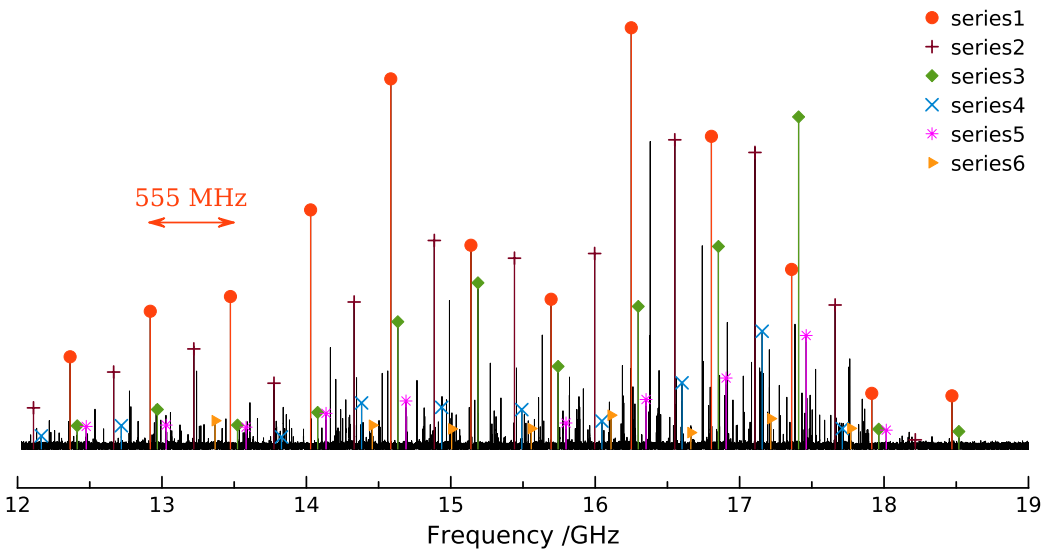

Figure S.14: Identification of six series of equally spaced transitions from the experimental spectrum.

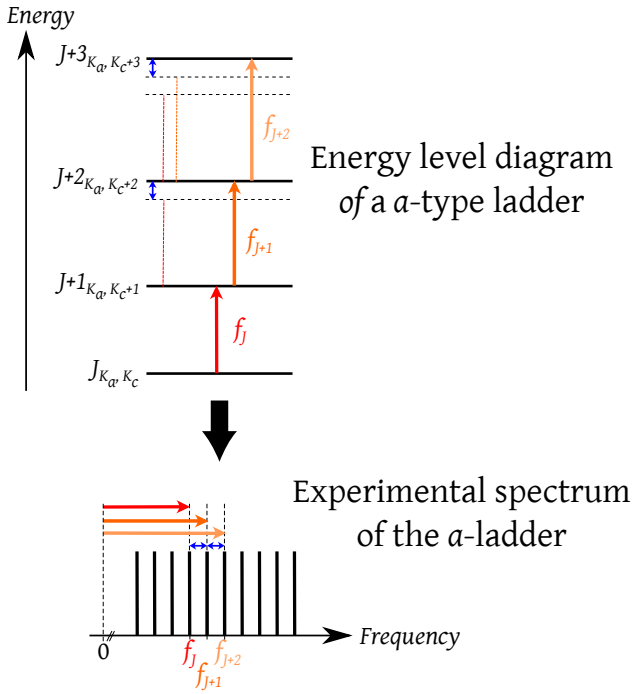

Figure S.15: Graphical representation of the energy level diagram of an a-type series and consequence on the experimental spectrum. The difference between two consecutive frequencies in the ladder is roughly constant, yielding equally spaced transitions on the experimental spectrum.

yielding the standard deviation plot presented in Figure S.16 (*top plot*), in which only the physically relevant cases are plotted ($A \geq B \geq C$ and fit that converged in 150 iterations maximum). Two fits converged to roughly the same standard deviation, at iterations 111 and 450. These two fits correspond to the assignments

$22_{0,22} - 21_{0,21}$ and $22_{1,22} - 21_{1,21}$, respectively, for the first transition of the series at 12363.832 MHz, a likely indication of unresolved asymmetric splitting ($K_a + K_c = J$ or $J+1$). The two fits converged toward similar values of C, similar values of B, but completely different values of A. Considering very limited information on the A rotational constant can be extracted from a single a-type series, especially when the frequency separation between consecutive lines in the series is almost constant as in the present case, this result is not surprising and we decided to assign both transitions of iterations 111 and 450 to the lines of series1, taking into account the unresolved asymmetric splitting. It should be noted that in the conventional use of the AMDOR algorithm, cross-ladder transitions (i.e. transitions linking two a-type series) are ideally used which constrains the fit and usually yields to convergence in a single iteration of the script. In the present case, this first step was not sufficient to determine all three rotational constants of the compound and more iterations of the AMDOR script were needed.

Table S.2: Rotational constants determined for the two bests iterations of the AMDOR procedure at the first step, i.e. for the assignment of series1.

	Iteration 111	Iteration 450
A	493(73)	849(119)
B	384(36)	317.4(82)
C	277.5588(42)	277.5635(57)

In the second step, the AMDOR algorithm was used on the transitions of the second strongest series in the experimental spectrum, series 2 (Figure S.14), while keeping the already assigned transitions of series1 from the first step. As with the previous series, two fits are distinguishable by their smaller standard deviation, at iterations 102 and 442, corresponding for the first transition of the series at 12110.361 MHz to quantum number assignments $21_{1,20} - 20_{1,19}$ and $21_{2,20} - 20_{2,19}$, respectively (Figure S.16, *middle trace*). As in the first step, these assignments were both added to the linelist accounting for the unresolved asymmetric splitting.

Finally, in a third step, the AMDOR procedure was performed once more on series3 (Figure S.14) while keeping the assignments of both series1 and series2 in the linelist. Again, two best iterations are easily distinguishable, at iterations 103 and 443 (Figure S.16, *bottom trace*) corresponding to the assignments $21_{2,19} - 20_{2,18}$ and $21_{3,19} - 20_{3,18}$ for the first line of the series at 12413.185 MHz. Remarkably, these two best AMDOR iterations converged toward the same rotational constants (Table S.3) thus confirming the unresolved asymmetric splitting on these three series of transitions.

Step 1:

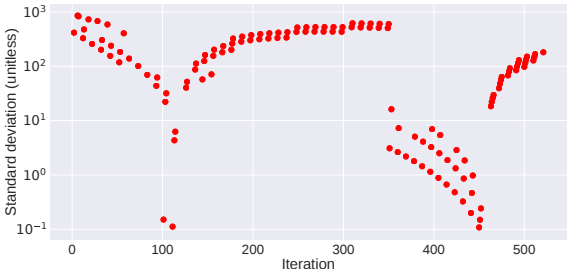

Step 2:

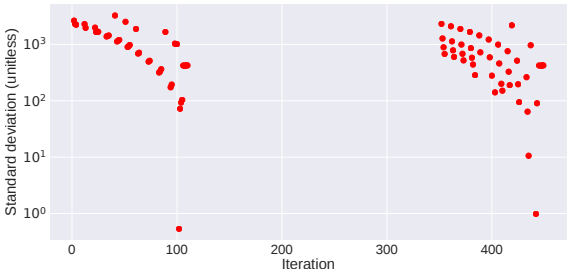

Step 3:

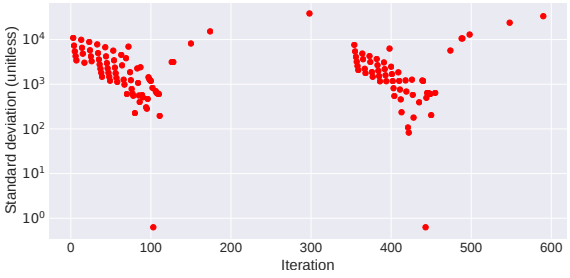

Figure S.16: Unitless standard deviation obtained at each step of assignment using the AMDOR procedure. The bests fits are identified by their smallest standard deviation. *From top to bottom:* series1, series1+2, series1+2+3.

Table S.3: Rotational constants determined for the two bests iterations of the AMDOR procedure at the third step, i.e. for the assignment of series1, series2, and series3.

	Iteration 103	Iteration 443
A	558.0(41)	558.2(41)
B	358.5(12)	358.4(12)
C	277.56942(78)	277.56943(79)

Using these constants, a prediction of the full a-type spectrum, using the `spcat` program from H. M. Pickett,[25] reproduced accurately not only the transitions already in the linelist but also series 4 and series 5, while predicting the close lines of series 6 (Figure S.17. These transitions were assigned and fit allowing to

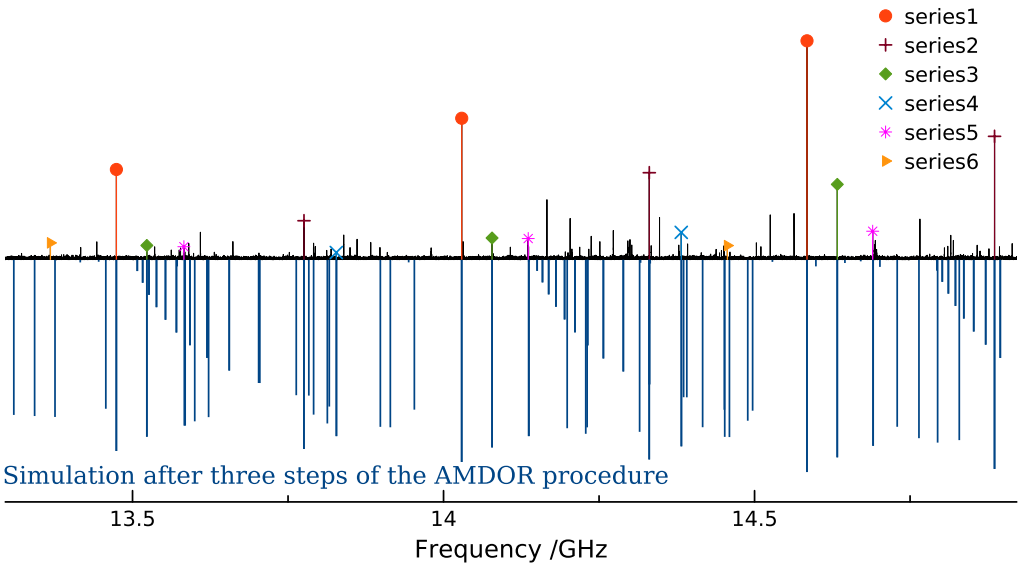

Figure S.17: Prediction of the *a*-type spectrum, in green, after three steps of the AMDOR procedure and comparison with the experimental spectrum.

subsequently assign both *b*- and *c*-type transitions in the experimental spectrum.

S.3.2 Spectroscopic Constants Determination

A total of 380 frequencies have been assigned to **1** from the experimental spectrum, for a total of 695 transitions. Besides the three A, B, C rotational constants, five quartic centrifugal distortion constants were required to reproduce the transitions at the experimental accuracy. Numerous experimental frequencies were assigned to the same experimental frequencies (from overlapping *a*-, *b*-, and/or *c*-type transitions and/or unresolved asymmetric splitting). In the final fit, each transition in the linelist was thus weighted according to its expected intensity at 10 K and assuming projected values of the dipole moments along the three moments of inertia of $\mu_a = 2.6$ D, $\mu_b = 2.3$ D, and $\mu_c = 0.8$ D (values obtained from the X-ray structure, *vide infra*). The individual weights were determined using the `calbak` program from H. M. Pickett.[25] The expected accuracy of each experimental line was estimated from the signal-to-noise ratio, the frequency step in the experimental spectrum (40 kHz), and the full width at half maximum of the lines ($\sim$ 200 kHz) yielding values ranging from 20 to 120 kHz.

The fit was performed using `spfit` and a Watson's *A*-type reduction in the I^r representation. The derived spectroscopic constants are reported in Table S.4. We note the excellent agreement between these final constants and those determined with only three iterations of the AMDOR procedure (see Table S.3).

Table S.4: Spectroscopic constants of **1** (in MHz) determined from the analysis of the microwave spectrum (gas phase value) and comparison with values derived from the crystal structure. Uncertainties (1σ) for the gas phase values are reported in the unit of the last significant digit.

Constant	Gas phase	Crystal	Ratio
A	553.80105(46)	521.28	1.06
B	359.73363(31)	365.13	0.99
C	277.57441(25)	272.30	1.02
$\Delta_J \times 10^6$	5.82(18)		
$\Delta_{JK} \times 10^3$	0.04126(64)		
$\Delta_K \times 10^3$	0.0838(15)		
$\delta_J \times 10^6$	1.26(10)		
$\delta_K \times 10^3$	0.0273(11)		

The final standard deviation of the fit is of 35 kHz, and a unitless value of 1.07, an indication that the estimated uncertainties for the experimental frequencies are reasonable. These constants allow the experimental frequencies of the spectrum to be nicely reproduced, as illustrated in Figure S.18. The relative intensities between the transitions show some disagreement which may arise from difference between the actual rotational temperature of **1** in the buffer gas cell and the 10 K value used for predicting the spectrum, as well as from slight difference between the actual dipole moments and the values used to predict the spectrum. After assigning transitions of **1**, and of SO_2, S_2O and SO (see main text), only a few weak experimental lines remained unidentified.

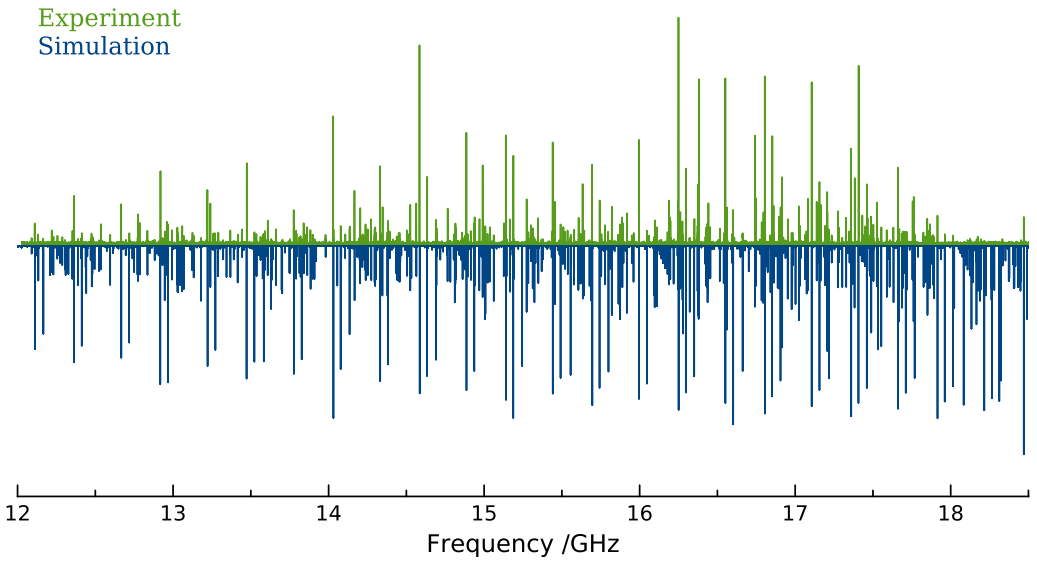

Figure S.18: Comparison between the experimental spectrum (top trace, in green) and the prediction (at 10 K, bottom trace, in blue) resulting from the final fit of transitions of **1**.

S.3.3 Structure of 1

Rotational constants of **1** have been derived from the X-ray structure of the compound (*vide infra*), and are compared with the gas phase rotational constants in Table S.4. Very interestingly, the *A*, *B*, and *C* are extremely close, indicating that **1** adopts a similar structure in the gas phase and as a crystalline solid.

S.3.4 General Remarks and Consequences

It is very interesting to note that the use of the AMDOR procedure has enabled the very fast assignment of the pure rotational spectrum of **1** in only a couple of hours from the identification of the series of the experimental spectrum to a final fit, especially without an *ab initio* prediction and associated rotational constants. As the unambiguous attribution of the rotational fingerprint of a compound (here a fairly large organic molecule) can now be performed without any initial knowledge of its molecular structure or elemental composition, microwave spectroscopy has the potential to complement the commonly used characterization techniques employed by synthetic chemists.

S.4 X-Ray Diffraction Studies

S.4.1 Data acquisition

The crystals were mounted in hydrocarbon oil on a nylon loop or a glass fiber. Low-temperature (100 K) data were collected on a Bruker-AXS X8 Kappa Duo diffractometer coupled to a Smart Apex2 CCD detector with Mo Kα radiation ($\lambda = 0.71073$ Å) with ϕ- and ω-scans. A semi-empirical absorption correction was applied to the diffraction data using SADABS.[26] All structures were solved by intrinsic phasing using SHELXT[27] and refined against F^2 on all data by full-matrix least squares with SHELXL-2015[28] using established methods. All non-hydrogen atoms were refined anisotropically. All hydrogen atoms were included in the model at geometrically calculated positions and refined using a riding model. The isotropic displacement parameters of all hydrogen atoms were fixed to 1.2 times the U_{eq} value of the atoms they are linked to (1.5 times for methyl groups). Descriptions of the individual refinements follow below and details of the data quality and a summary of the residual values of the refinements for all structures are given in Table S.5. Further details can be found in the form of .cif files available from the CCDC.

Table S.5: Crystallographic Data for **1** and **2**

	1	$[Na_2(DME)_3][Ru(N_4Me_8)(SO)]$
Reciprocal Net code / CCDC	X8_16220 / CCDC 1567576	X8_16221 / CCDC 1567577
Empirical formula, FW (g/mol)	$C_{14}H_{10}N_2OS$, 254.30	$C_{28}H_{44}N_{2.67}Na_{1.33}O_5 5Ru_{0.67}$, 617.40
Color / Morphology	Colorless / Needle	Orange / Block
Crystal size (mm^3)	$0.200 \times 0.100 \times 0.040$	$0.115 \times 0.099 \times 0.042$
Temperature (K)	100(2)	100(2)
Wavelength (Å)	0.71073	0.71073
Crystal system, Space group	Orthorombic, Iba2	Monoclinic, C2/c
Unit cell dimensions (Å, °)	$a = 14.9840(16)$, $\alpha = 90$	$a = 24.271(2)$, $\alpha = 90$
	$b = 21.409(2)$, $\beta = 90$	$b = 18.9482(15)$, $\beta = 107.9930(10)$
	$c = 7.2226(8)$, $\gamma = 90$	$c = 21.0348(17)$, $\gamma = 90$
Volume ($Å^3$)	2317.0(4)	9200.6(13)
Z	8	12
Density (calc., g/cm^3)	1.458	1.337
Absorption coefficient (mm^{-1})	0.266	0.457
$F(000)$	1056	3904
Theta range for data collection (°)	1.659 to 28.348	1.390 to 28.356
Index ranges	$-19 \leq h \leq 19$, $-28 \leq k \leq 28$,	$-32 \leq h \leq 30$, $0 \leq k \leq 25$,
	$-28 \leq -9 \leq 9$	$0 \leq l \leq 28$
Reflections collected	21197	14061
Independent reflections, R_{int}	2861, 0.0617	14061,
Completeness to θ_{max} (%)	99.8	100.0
Absorption correction	Semi-empirical from equiv.	Semi-empirical from equiv.
Refinement method	Full-matrix least-squares on F^2	Full-matrix least-squares on F^2
Data / Restraints / Parameters	2861 / 1 / 163	14061 / 232 / 602
Goodness-of-fit[a]	1.055	1.044
Final R indices[b] $[I > 2\sigma(I)]$	$R_1 = 0.0374$, $wR_2 = 0.0853$	$R_1 = 0.0500$, $wR_2 = 0.1069$
R indices[b] (all data)	$R_1 = 0.0476$, $wR_2 = 0.0908$	$R_1 = 0.0795$, $wR_2 = 0.1206$
Largest diff. peak and hole ($e \cdot Å^{-3}$)	0.231 and −0.402	0.698 and −0.710

[a] GooF = $\sqrt{\frac{\Sigma[w(F_o^2-F_c^2)^2]}{(n-p)}}$ [b] $R_1 = \frac{\Sigma||F_o|-|F_c||}{\Sigma|F_o|}$; $wR_2 = \sqrt{\frac{\Sigma[w(F_o^2-F_c^2)^2}{\Sigma[w(F_o^2)^2]}}$; $w = \frac{1}{\sigma^2(F_o^2)+(aP)^2+bP}$; $P = \frac{2F_c^2+\max(F_o^2,0)}{3}$

S.5 Computational Details

All calculations were performed with the ORCA 4.0.0 quantum chemistry package from the development team at the University of Bonn.[29,30]

S.5.1 Comparison of Precursor Thermodynamics

These calculations were performed using ORCA keywords `B3LYP D3BJ Def2-TZVP TightSCF Grid5 FinalGrid6 Opt TightOpt Freq`. This indicates the B3LYP density functional[31] with the Def2-TZVP basis set[32,33] in combination with D3(BJ) dispersion correction.[34] In all cases, computed electronic energies were corrected for zero-point energy, thermal energy, and entropic effects to obtain the enthalpy and free energy (all free energies reported at 298.15 K). All geometries had zero imaginary frequency vibrations. A model frustrated Lewis pair (FLP) precursor was used, which changed C_6F_5 substituents to CF_3, and mesityl or *p*-tolyl to CH_3.

S.5.2 Mechanistic Investigation of the Fragmentation of 1

These calculations were performed either using ORCA keywords `B3LYP D3BJ Def2-TZVP TightSCF Grid5 FinalGrid6 Opt TightOpt Freq` or using ORCA keywords `RI-B2PLYP D3BJ Def2-TZVP Def2-TZVP/C TightSCF Grid5 FinalGrid6 Opt TightOpt NumFreq`. The first set of keywords indicates the B3LYP density functional[31] with the Def2-TZVP basis set[32,33] in combination with D3(BJ) dispersion correction.[34] The second set of keywords indicates the double hybrid B2PLYP[35] rather than B3LYP. In all cases, computed electronic energies were corrected for zero-point energy, thermal energy, and entropic effects to obtain the enthalpy and free energy (all free energies reported at 298.15 K). All geometries had no spurious imaginary frequency vibrations.

S.5.3 Nudged Elastic Band Calculations

The minimum energy path for fragmentation of **1** was traced at the B3LYP-D3(BJ)/Def2-SVP level of theory with a nudged elastic band calculation using the Atomic Simulation Environment (ASE) python library[36] interfaced to ORCA 4.0.0. The nudged elastic band was constructed with 40 frames and a uniform spring constant of 0.1 eV/Å. The FIRE optimizer[37] was used with the climbing image algorithm[38] and a convergence criterion of 0.1 eV/Å. The initial and final geometries were taken from the B3LYP-D3(BJ)/Def2-TZVP

calculations described above. No hidden stationary points were uncovered in this sweep of the minimum energy pathway, as is illustrated in Figure S.19.

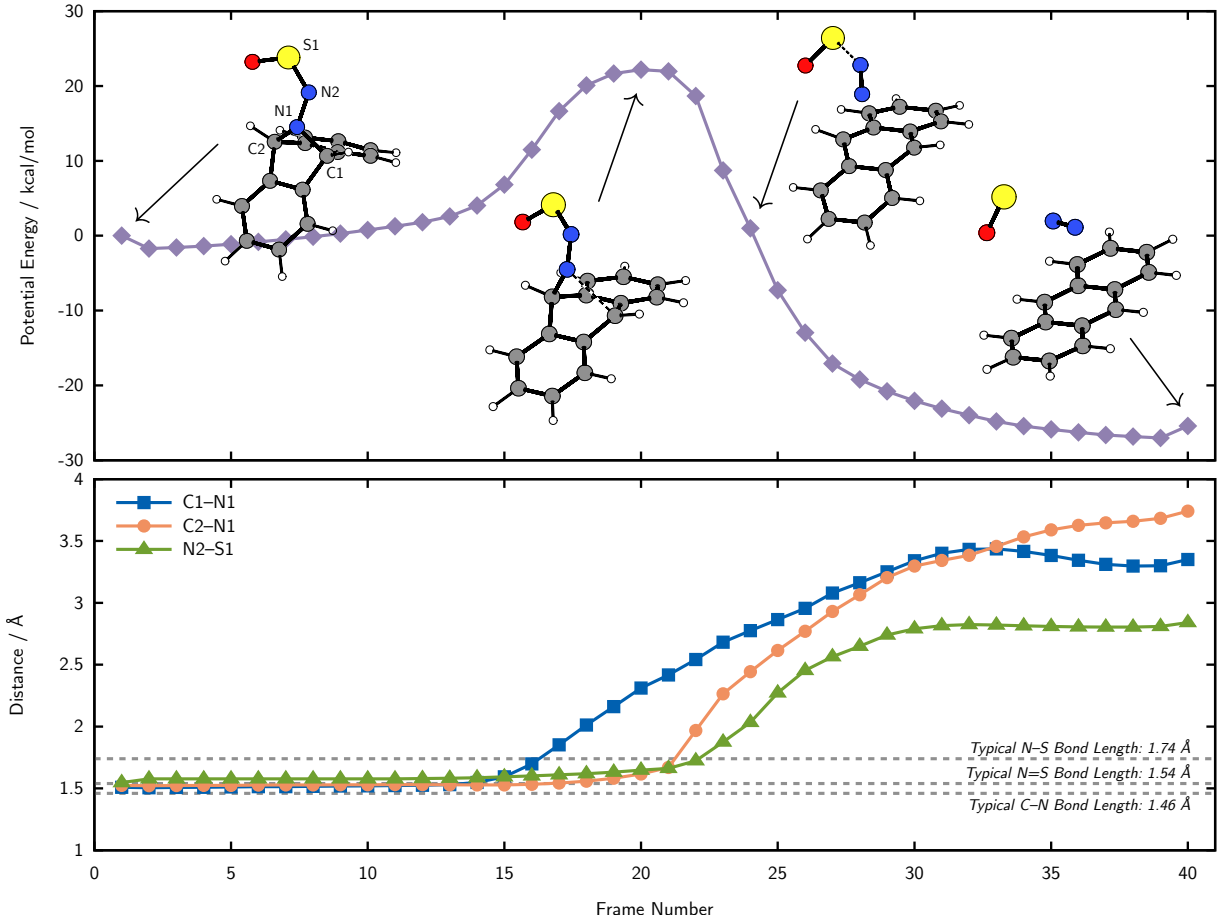

Figure S.19: Results of a nudged elastic band refinement of the minimum energy path for fragmentation of **1** through the located transition state. No hidden stationary points are uncovered.

S.6 Construction and Use of a Gas-IR cell

In order to analyze by gas-phase IR spectroscopy the gases evolved from **1** upon thermal decomposition, a gas-IR cell was employed. The cell was constructed from 1" OD, 0.6875" ID heavy-walled borosilicate glass tubing (Chemglass Life Sciences). An 8" length of tubing was cut and two glass stopcock valves were attached to the two ends. The two openings of the tube were closed with calcium fluoride windows (Edmund optics, 47-683, 25 mm diameter, 3 mm thickness) using epoxy glue. The epoxy is a special blend (Epotek, 353ND) for attaching optic devices to glass and was cured at 150 °C for 1 hour. The calcium fluoride windows have high transparency from 80 000 cm^{-1} to 1000 cm^{-1}. A schematic drawing and a photo of the cell are shown below (Figure S.20 and Figure S.21, respectively).

During routine usage, the cell was usually attached between a reaction vessel and a Schlenk line. The cell was evacuated and the gases were then pulled into the cell from the reaction vessel by static vacuum.

A slightly modified cell, which is mostly identical to the one described above, but features an additional 14/20 ground-glass joint and a small glass pocket directly below the joint on the opposite side of the tube was employed as well. Gases were introduced into the nitrogen-purged cell compartment through a rubber septum using a syringe with a needle, or were generated directly in the evacuated cell by thermal decomposition of a solid sample (about 10 mg) placed into the glass pocket. A photo of this cell is shown below (Figure S.22).

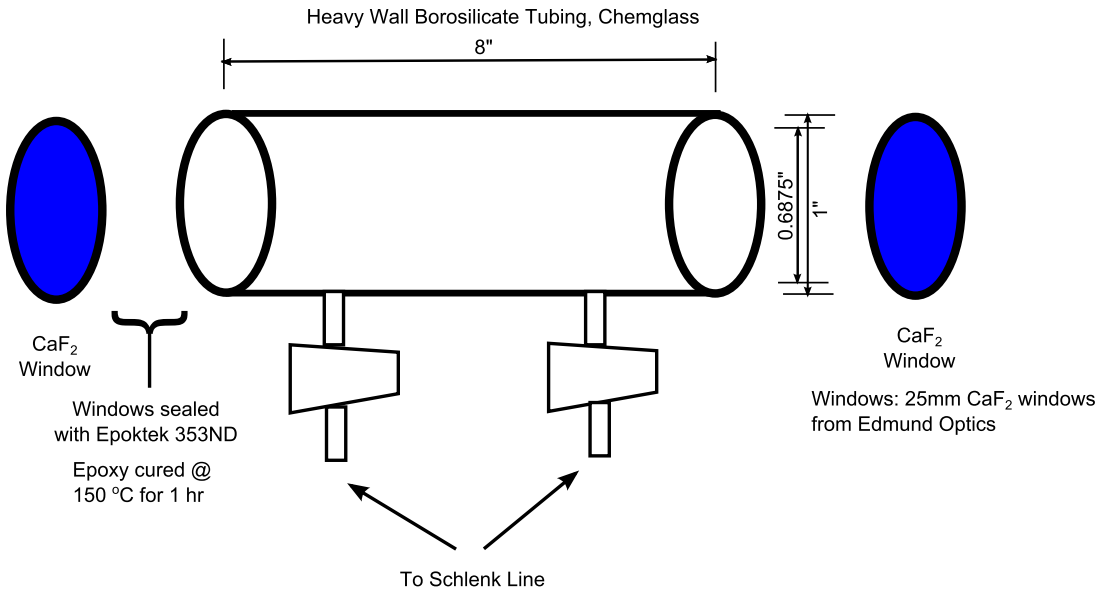

Figure S.20: A schematic of the gas IR cell.

Figure S.21: A photograph of the gas IR cell.

Figure S.22: A photograph of the modified gas IR cell used for the generation and analysis of gases evolving from a solid sample (placed into the glass pocket) by thermal decomposition.

References

[1] Pangborn, A. B.; Giardello, M. A.; Grubbs, R. H.; Rosen, R. K.; Timmers, F. J. *Organometallics* **1996**, *15*, 1518–1520.

[2] Williams, D. B. G.; Lawton, M. *J. Org. Chem.* **2010**, *75*, 8351–8354.

[3] Carpino, L. A.; Padykula, R. E.; Barr, D. E.; Hall, F. H.; Krause, J. G.; Dufresne, R. F.; Thoman, C. J. *J. Org. Chem.* **1988**, *53*, 2565–2572.

[4] Campion, B. K.; Heyn, R. H.; Tilley, T. D. *J. Chem. Soc., Chem. Commun.* **1988**, 278–280.

[5] Bonomo, L.; Solari, E.; Scopelliti, R.; Floriani, C. *Angew. Chem. Int. Ed.* **2001**, *40*, 2529–2531.

[6] Fulmer, G. R.; Miller, A. J. M.; Sherden, N. H.; Gottlieb, H. E.; Nudelman, A.; Stoltz, B. M.; Bercaw, J. E.; Goldberg, K. I. *Organometallics* **2010**, *29*, 2176–2179.

[7] Ammann, C.; Meier, P.; Merbach, A. *J. Magn. Reson.* **1982**, *46*, 319–321.

[8] Townsend, T. M.; Allanic, A.; Noonan, C.; Sodeau, J. R. *J. Phys. Chem. A* **2012**, *116*, 4035–4046.

[9] Mass Spec Data Center, S. S., director *NIST Chemistry WebBook, NIST Standard Reference Database 69*; National Institute of Standards and Technology: Gaithersburg MD, 20899, 2017.

[10] Velian, A.; Nava, M.; Temprado, M.; Zhou, Y.; Field, R. W.; Cummins, C. C. *J. Am. Chem. Soc.* **2014**, *136*, 13586–13589.

[11] De Jongh, D. C.; Van Fossen, R. Y. *J. Org. Chem.* **1972**, *37*, 1129–1135.

[12] Schenk, W. A.; Leißner, J. *Z. Naturforsch., B: Chem. Sci.* **1987**, *42*, 799–800.

[13] Grainger, R. S.; Patel, B.; Kariuki, B. M.; Male, L.; Spencer, N. *J. Am. Chem. Soc.* **2011**, *133*, 5843–5852.

[14] Nakayama, J.; Tajima, Y.; Xue-hua, P.; Sugihara, Y. *J. Am. Chem. Soc.* **2007**, *129*, 7250–7251.

[15] Schenk, W. A.; Karl, U. *Z. Naturforsch., B: Chem. Sci.* **1989**, *44*, 988–989.

[16] McCarthy, M. C.; Travers, M. J.; Kovács, A.; Gottlieb, C. A.; Thaddeus, P. *Astrophys. J., Suppl. Ser.* **1997**, *113*, 105.

[17] McCarthy, M. C.; Chen, W.; Travers, M. J.; Thaddeus, P. *Astrophys. J., Suppl. Ser.* **2000**, *129*, 611–623.

[18] Ellenbroek, A. W.; Dymanus, A. *Chem. Phys. Lett.* **1976**, *42*, 303–306.

[19] Thorwirth, S.; Theulé, P.; Gottlieb, C. A.; Müller, H. S. P.; McCarthy, M. C.; Thaddeus, P. *J. Mol. Struct.* **2006**, *795*, 219–229.

[20] Amano, T.; Hirota, E.; Morino, Y. *J. Phys. Soc. Jpn.* **1967**, *22*, 399–412.

[21] Clark, W. W.; De Lucia, F. C. *J. Mol. Spectrosc.* **1976**, *60*, 332–342.

[22] Patterson, D.; Doyle, J. M. *Mol. Phys.* **2012**, *110*, 1757–1766.

[23] Brown, G. G.; Dian, B. C.; Douglass, K. O.; Geyer, S. M.; Shipman, S. T.; Pate, B. H. *Rev. Sci. Instrum.* **2008**, *79*, 053103.

[24] Martin-Drumel, M.-A.; McCarthy, M. C.; Patterson, D.; McGuire, B. A.; Crabtree, K. N. *J. Chem. Phys.* **2016**, *144*, 124202.

[25] Pickett, H. M. *J. Mol. Spectrosc.* **1991**, *148*, 371–377.

[26] (a) Bruker, SADABS. 2008; (b) Krause, L.; Herbst-Irmer, R.; Sheldrick, G. M.; Stalke, D. *J. Appl. Crystallogr.* **2015**, *48*, 3–10.

[27] (a) Sheldrick, G. M.; Schneider, T. R. In *[16] SHELXL: High-Resolution Refinement*; in Enzymology, B. M., Ed.; Macromolecular Crystallography Part B; Academic Press, 1997; Vol. 277; pp 319–343; (b) Sheldrick, G. M. *Acta Crystallogr., Sect. A: Found. Crystallogr.* **2008**, *64*, 112–122.

[28] Sheldrick, G. M. *Acta Crystallogr., Sect. C: Cryst. Struct. Commun.* **2015**, *71*, 3–8.

[29] Neese, F. *WIREs Comput. Mol. Sci.* **2012**, *2*, 73–78.

[30] Neese, F. *WIREs Comput. Mol. Sci.* **2017**, 1–6.

[31] (a) Becke, A. D. *Phys. Rev. A* **1988**, *38*, 3098–3100; (b) Lee, C.; Yang, W.; Parr, R. G. *Phys. Rev. B* **1988**, *37*, 785–789.

[32] Schäfer, A.; Huber, C.; Ahlrichs, R. *J. Chem. Phys.* **1992**, *97*, 2571–2577.

[33] Weigend, F.; Ahlrichs, R. *Phys. Chem. Chem. Phys.* **2005**, *7*, 3297–3305.

[34] (a) Grimme, S.; Antony, J.; Ehrlich, S.; Krieg, H. *J. Chem. Phys.* **2010**, *132*, 154104; (b) Grimme, S.; Ehrlich, S.; Goerigk, L. *J. Comput. Chem.* **2011**, *32*, 1456–1465.

[35] Grimme, S. *J. Chem. Phys.* **2006**, *124*, 034108.

[36] Hjorth Larsen, A. et al. *J. Phys. Condens. Matter* **2017**, *29*, 273002.

[37] Bitzek, E.; Koskinen, P.; Gähler, F.; Moseler, M.; Gumbsch, P. *Phys. Rev. Lett.* **2006**, *97*, 170201.

[38] Henkelman, G.; Uberuaga, B. P.; Jónsson, H. *J. Chem. Phys.* **2000**, *113*, 9901–9904.